Journal of Wind Engineering & Industrial Aerodynamics 211 (2021) 104556

Contents lists available at ScienceDirect

Journal of Wind Engineering & Industrial Aerodynamics

journal homepage: www.elsevier.com/locate/jweia

# Numerical study of dynamic response of railway vehicles under tunnel exit winds using multibody dynamic simulations

Takeshi Ishihara [a], Dongqin Zhang [a,*], Yosuke Nagumo [b]

[a] Department of Civil Engineering, School of Engineering, The University of Tokyo, Tokyo, Japan
[b] Safety Research Laboratory, Research and Development Center of JR East Group, East Japan Railway Company, Saitama, Japan

ARTICLE INFO

*Keywords:*
Railway vehicle
Tunnel exit wind
Dynamic response
Quasi-static analysis
Multibody dynamic simulation
Dynamic amplification factor

ABSTRACT

The dynamic responses of railway vehicles under crosswinds are investigated by using multibody dynamic simulations and compared with the experimental data. A new gust model is also proposed to predict aerodynamic forces acting on railway vehicles under tunnel exit winds. The dynamic responses of a model vehicle under tunnel exit winds are firstly predicted by multibody dynamic simulations and the predicted rolling angles of the vehicle by the identified structural parameters show good agreement with those from the running vehicle test. The dynamic responses of a commuter rail under natural winds are then studied and the calculated wheel unloading ratios match favorably with those from the field test. Finally, a dynamic amplification factor (DAF) for railway vehicles under tunnel exit winds is proposed and systematically investigated. It is found that DAF decreases as the passing time as well as the damping ratio and natural frequency of railway vehicle increase. A simple formula is also proposed to predict DAF of railway vehicles under tunnel exit winds.

## 1. Introduction

Recently, railway vehicles have shown trends of high-speed and lightweight, which conserve energy, reduce rail damage and wheel wear, improve transportation capacity. However, these developments may have a negative effect on crosswind stability of railway vehicles.

In the last decades, many researches have been carried out to investigate aerodynamic characteristics and the dynamic behavior of railway vehicles under crosswinds (Baker et al., 2009). In general, in order to assess the crosswind stability of railway vehicles, aerodynamic coefficients of railway vehicles were firstly evaluated by wind tunnel tests (Bocciolone et al., 2008; Cheli et al., 2013; Kikuchi and Suzuki, 2015; Schober et al., 2010; Suzuki and Hibino, 2016), CFD simulations (Cheli et al., 2010; Premoli et al., 2016) and the moving wind tunnel test (Dorigatti et al., 2015). Some full-scale experiments (Baker et al., 2004; Suzuki and Hibino, 2016) were also carried out to study aerodynamic characteristics of railway vehicles. Then, the steady wind, or the turbulent wind of a moving railway vehicle generated by PSD (Cheli et al., 2012; Li et al., 2017; Hu et al., 2019) was widely used to calculate aerodynamic forces by the quasi-steady theory. The aerodynamic admittance in frequency domain or the weighting function in time domain which shows the spatial correlation of wind on the railway vehicles was adopted to modify quasi-static theory (Sterling et al., 2009; Tomasini and Cheli, 2013). The 3-s average wind speed method was also introduced to evaluate the spatial correlation of wind by Nagumo and Ishihara (2020). Finally, dynamic responses of railway vehicles under crosswinds were evaluated by either the quasi-static analysis (Baker, 2013; Hibino et al., 2010) or multibody dynamic simulations (Cheli et al., 2012; You et al., 2018; Liu et al., 2020).

In addition, numerous railway lines are constructed in mountainous areas and it is likely that the railway vehicle is being attacked by crosswinds simultaneously when it is running out of the tunnel. At this moment, aerodynamic forces acting on the railway vehicle and the corresponding dynamic responses increase rapidly as the vehicle passes through the tunnel exit which are totally different from those under steady winds or turbulent winds. It implies that accurate assessment of aerodynamic forces and dynamic responses of railway vehicles under tunnel exit winds are necessary.

In the European standard (EN 14067-6, 2010), aerodynamic forces caused by unsteady winds can be calculated by the Chinese hat gust model and the quasi-steady theory. The temporal wind at the vehicle center is low-pass filtered by the centered moving average method with a window size of vehicle length. However, the low-pass filter based on the centered moving average method has not been validated. The unsteady aerodynamic forces on the railway vehicle were calculated by CFD simulations (Thomas et al., 2010b) and measured by wind tunnel tests (Hibino et al., 2013a), in which the calculated and measured unsteady

* Corresponding author.
*E-mail address:* dongqin.zhang@outlook.com (D. Zhang).

https://doi.org/10.1016/j.jweia.2021.104556
Received 3 August 2020; Received in revised form 29 January 2021; Accepted 29 January 2021
Available online xxxx
0167-6105/© 2021 Elsevier Ltd. All rights reserved.

**Nomenclature**

| | |
|---|---|
| $a$ | decay factor of DAF |
| $A$ | side area of car body |
| $A_{exp}$ | averaged amplitude of rolling angle measured by experiment |
| $A_{sim}$ | averaged amplitude of rolling angle calculated by MBS |
| $A_{sl}$ | amplitude of sinusoidal force |
| $b$ | exponent of $\Delta t$ |
| $B_{sl}$ | frequency of sinusoidal force |
| $C_L$ | lift force coefficient |
| $C_M$ | rolling moment coefficient |
| $C_S$ | side force coefficient |
| $C_{Si}$ | side force coefficient of the *ith* strip |
| $C_{sl}$ | phase of sinusoidal force |
| $c$ | cant |
| $D$ | wheel unloading ratio |
| $DAF$ | dynamic amplification factor |
| $D_{dynamic}$ | dynamic wheel unloading ratio |
| $D_{static}$ | static wheel unloading ratio |
| $D_{ys}$ | lateral damping parameter in second suspension |
| $D_{zs}$ | vertical damping parameter in second suspension |
| $e$ | height between gravity of car body and wind force center |
| $f_n$ | natural frequency of railway vehicle |
| $F_L(t)$ | lift force |
| $F_S(t)$ | side force |
| $F_u$ | excessive centrifugal force acting on car body |
| $F_u^{'}$ | excessive centrifugal force acting on bogie |
| $F_V$ | lateral force caused by the track irregularity |
| $F_V^{'}$ | sinusoidal lateral force |
| $g$ | gravitational acceleration |
| $G$ | distance between two wheel-rail contact points |
| $h_1$ | distance between gravity of car body and axle spring |
| $h_2$ | height between gravity of car body and air spring |
| $h_{BC}$ | height of wind force center |
| $h_c$ | height of the center of car body |
| $h_{GB}$ | height of gravity of car body |
| $h_{GT}$ | height of gravity of bogie |
| $H_0$ | height of car body |
| $K_{ys}$ | lateral stiffness in second suspension |
| $K_{zs}$ | vertical stiffness in second suspension |
| $K_{zs2}$ | stiffness of vertical bump stop |
| $L$ | gust duration |
| $L_0$ | length of car body |
| $m_B$ | mass of car body |
| $m_T$ | mass of bogie including two wheelsets |
| $m_T^{'}$ | mass of bogie |
| $m_W$ | mass of wheelset |
| $M_R(t)$ | rolling moment |
| $M_{O.C}(t)$ | calculated overturning moment |
| $M_{O.M}(t)$ | measured overturning moment |
| $N$ | the total number of strips |
| $P_0$ | static wheel loading |
| $P_{exp}$ | averaged period of rolling angle measured by experiment |
| $P_{sim}$ | averaged period of rolling angle calculated by MBS |
| $P_L$ | wheel loading at windward side |
| $R$ | curve radius |
| $R(T)$ | ratio of the maximum measured and calculated overturning moment at every 60 s |
| $t$ | time |
| $T$ | time interval (60 s) |
| $U_0$ | gust amplitude |
| $u_{3s-gust}(t)$ | 3-s average wind speed |
| $u_{i,inst}(t)$ | instantaneous wind speed of the No. $i$ anemometer |
| $u_{inst}(t)$ | instantaneous wind speed |
| $u_{sa}(t)$ | spatial average wind speed |
| $v_a(t)$ | resultant wind speed |
| $v_c(t)$ | the temporal wind speed at the vehicle center |
| $V_{tr}$ | train velocity |
| $v_{wi}$ | wind speed at the *ith* strip |
| $y_2$ | lateral displacement of car body relative to air spring |
| $y_B$ | lateral displacement of car body |
| $z_B$ | vertical displacement of car body |

*Greek symbols*

| | |
|---|---|
| $\beta(t)$ | angle of attack for the resultant wind |
| $\beta_w$ | angle of attack for wind |
| $\Delta t$ | passing time |
| $\zeta$ | total equivalent damping ratio |
| $\zeta_l$ | lateral equivalent damping ratio |
| $\zeta_v$ | vertical equivalent damping ratio |
| ρ | air density |
| $\varphi_1$ | rolling angle of car body about axle spring |
| $\varphi_2$ | rolling angle of car body about air spring |
| $\varphi_B$ | rolling angle of the of car body |

aerodynamic forces were directly used to simulate the dynamic responses of the vehicle under tunnel exit winds. However, these approaches have some limitations, the calculated and measured forces can only be used for the railway vehicles in the tests. An alternative method was proposed by using by the sum of wind force on the surface of structure and applied to simulate instantaneous aerodynamic forces caused by tornado winds (Liu et al., 2018). This indicates that an accurate wind model to evaluate unsteady aerodynamic forces acting on railway vehicles caused by tunnel exit winds is still necessary, although there are some methods which has been used to calculate aerodynamic forces included by unsteady winds.

Moreover, the dynamic responses of railway vehicles under cross-winds are generally calculated by multibody dynamic simulations. The dynamic responses of railway vehicles under unsteady winds were carried out by the experiment (Thomas et al, 2010a, 2015) and numerical simulations (Thomas et al., 2010b). They showed that the wheel unloading increased even if aerodynamic forces tended to be constant values. This phenomenon was also observed in the numerical simulation of crosswind response of high-speed train under Chinese hat gust (Sesma et al., 2012; You et al., 2018). The dynamic response of railway vehicles changed with the ramp time of the wind speed and was affected significantly when the ramp time was between zero and 1 s (Liu et al, 2019, 2020). These researches concluded that dynamic responses of railway vehicles in tunnel exit winds would be larger than that in steady winds even if the maximum wind speed is the same. The calculated wheel unloading ratio considering the dynamic effect of railway vehicle under tunnel exit winds was larger than that obtained by the quasi-static analysis, and this amplification became obvious when the train velocity increased (Hibino et al., 2013a). It implies that the dynamic response of railway vehicles under tunnel exit winds is amplified and a simple formula is necessary to evaluate the dynamic amplification effect by the tunnel exit winds.

In this study, dynamic responses of railway vehicles under tunnel exit winds are investigated and a dynamic amplification factor is proposed to evaluate the dynamic effect caused by tunnel exit winds. Section 2 describes the numerical models, namely, the wind load model, quasi-static analysis, multibody dynamic simulations, and dynamic amplification

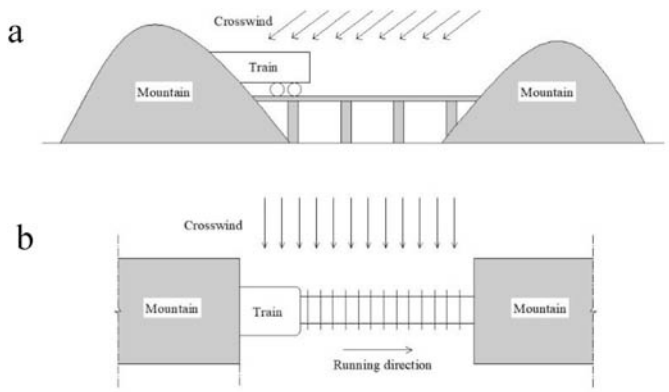


**Fig. 1.** A railway vehicle running out of the tunnel under crosswind conditions: (a) side view; (b) top view.

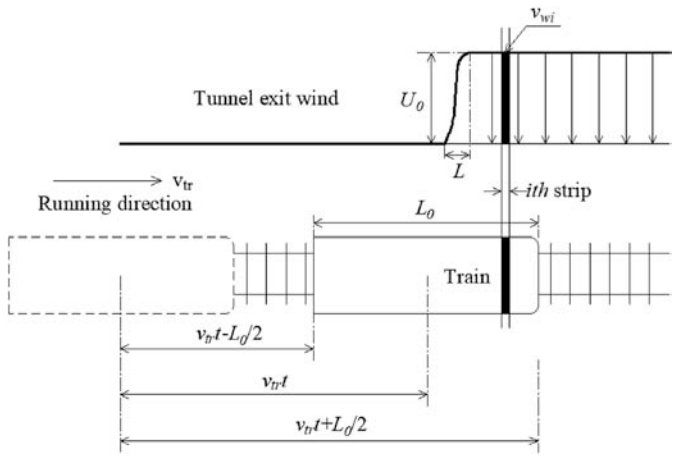


**Fig. 2.** Description of the tunnel exit wind model (top view).

factor. In section 3, dynamic responses of a scale model vehicle and a commuter rail are investigated and compared with the experimental data. The dynamic amplification factors of railway vehicles in tunnel exit winds are systematically investigated and a simple formula to evaluate DAF is proposed. Section 4 summarizes conclusions.

## 2. Numerical models

Wind load models are presented in section 2.1. The quasi-static analysis and multibody dynamic simulations are interpreted in section 2.2 and section 2.3, respectively. A dynamic amplification factor is proposed in section 2.4.

### 2.1. Wind load model

When a railway vehicle is running out of a tunnel, crosswinds attack the vehicle simultaneously as shown in Fig. 1. The wind speed at the tunnel exit increases rapidly from zero to the maximum wind speed due to the surface roughness of the mountain, and it maintains a constant value when the railway vehicle runs far away from the tunnel exit. The variation of wind speed is opposite when a railway vehicle is moving into a tunnel.

This variation of wind speed at the tunnel exit can be described by a gust model, such as one-minus-cosine model for airplanes (Hoblit, 1988), Chinese hat gust model for railway vehicles (EN 14067-6, 2010) and extreme wind model for wind turbines (IEC 61400-1, 2019). The one-minus-cosine gust model is coherent with the quasi-steady theory, while Chinese hat gust model with an exponential form leads to exaggerated time histories of aerodynamic forces (Carrarini, 2007). In this study, the one-minus-cosine gust wind is adopted to describe the wind speed at the tunnel exit. It is assumed that the tunnel exit wind is distributed along the track and perpendicular to the track as shown in Fig. 2. Then, the temporal wind speed at the vehicle center $v_c(t)$ as presented in Fig. 3(a) is low-pass filtered by the centered moving average method (EN 14067-6, 2010) and it is expressed as:

$$v_c(t) = \frac{\int_{\left(V_{tr}t-\frac{L_0}{2}\right)}^{\left(V_{tr}t+\frac{L_0}{2}\right)} v_{wi}dx}{L_0}, \quad i = 1\cdots N \tag{1}$$

where $V_{tr}$ is the train velocity and $t$ refers to time. $L_0$ represents the vehicle length and $v_{wi}$ shows the wind speed at the *ith* strip. $N$ is the total

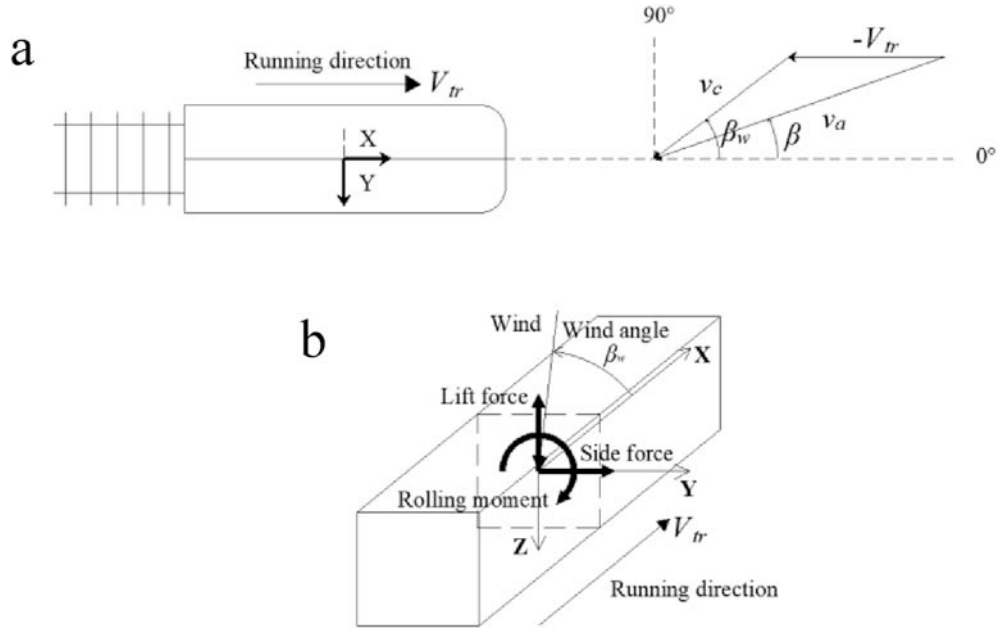


**Fig. 3.** Coordinate system for a railway vehicle: (a) wind direction; (b) directions of aerodynamic forces.

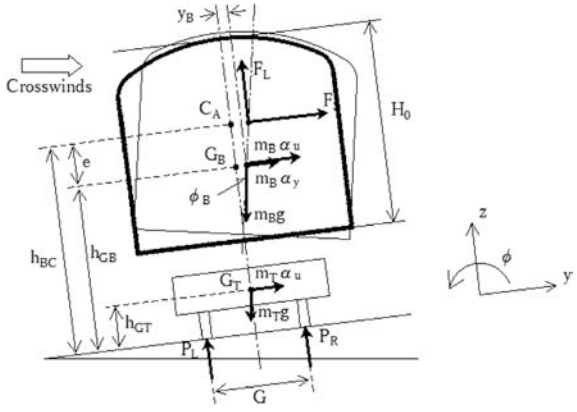


**Fig. 4.** A two-dimensional vehicle model used in the quasi-static analysis.

number of strips.

A new gust model is derived by the equivalent wind force method and used to transform the spatial distribution of wind speed to the temporal wind speed at the vehicle center. The total side force $F(t)$ on the vehicle can be calculated by Eq. (2) when the side area of railway vehicle is divided equidistantly into $N$ strips.

$$F(t)=\int_{\left(V_{tr}t-\frac{L_0}{2}\right)}^{\left(V_{tr}t+\frac{L_0}{2}\right)}\frac{1}{2}\rho C_{Si}H_0\left(v_{wi}^2+V_{tr}^2\right)dx,\quad i=1\cdots N \tag{2}$$

where $L_0$ is the length of car body, $V_{tr}$ is the train velocity and $v_{wi}$ is the wind speed at the *ith* strip as shown in Fig. 2. $H_0$ represents the height of car body as illustrated in Fig. 4. $C_{Si}$ corresponds to the side force coefficient of the *ith* strip. $t$ refers to time and $\rho$ is air density. $N$ shows the total number of strips.

The total side force $F(t)$ can also be calculated by Eq. (3) if the temporal wind speed at the vehicle center is expressed as $v_c(t)$ and the angle of attack for wind $\beta_w$ as illustrated in Fig. 3(a) is 90°.

$$F(t)=\frac{1}{2}\rho C_S L_0 H_0\left(v_c^2+V_{tr}^2\right) \tag{3}$$

where $v_c$ is the temporal wind speed at the vehicle center as shown in Fig. 3(a) and described in Eq. (4). $C_S$ corresponds to the side force coefficient of the vehicle.

In fact, these two expressions for the total side force on the vehicle should be equal and the temporal wind speed at the vehicle center can be derived from Eq. (2) and Eq. (3), if the aerodynamic coefficient for each strip has the same value as that for the whole vehicle and the railway vehicle passes through the tunnel exit wind at a constant velocity. In this study, the temporal wind speed at the vehicle center is calculated as:

$$v_c(t)=\sqrt{\frac{\int_{\left(V_{tr}t-\frac{L_0}{2}\right)}^{\left(V_{tr}t+\frac{L_0}{2}\right)}v_{wi}^2dx}{L_0}},\quad i=1\cdots N \tag{4}$$

The resultant wind speed $v_a(t)$ and the angle of attack for the resultant wind speed $\beta(t)$ as shown in Fig. 3(a) are calculated by using the temporal wind speed $v_c(t)$ and are expressed as:

$$v_a(t)=\sqrt{\left[V_{tr}+v_c(t)cos\beta_w\right]^2+\left[v_c(t)sin\beta_w\right]^2} \tag{5}$$

$$\beta(t)=arctan\left[\frac{v_c(t)sin\beta_w}{V_{tr}+v_c(t)cos\beta_w}\right] \tag{6}$$

where $\beta_w$ represents the angle of attack for wind.

The side force $F_S(t)$, lift force $F_L(t)$ and rolling moment $M_R(t)$ as shown in Fig. 3(b) are calculated by the quasi-steady theory and are presented as:

$$F_S(t)=\frac{1}{2}\rho AC_s(\beta(t))v_a^2(t) \tag{7}$$

$$F_L(t)=\frac{1}{2}\rho AC_L(\beta(t))v_a^2(t) \tag{8}$$

$$M_R(t)=\frac{1}{2}\rho AC_M(\beta(t))v_a^2(t)H_0 \tag{9}$$

where $\rho$ is air density and $A$ represents the side area of car body. $C_s(\beta(t))$, $C_L(\beta(t))$ and $C_M(\beta(t))$ are aerodynamic coefficients. $v_a(t)$ is the resultant wind speed as shown in Fig. 3(a).

### 2.2. Quasi-static analysis

A quasi-static analysis to evaluate the critical wind speed of railway vehicles overturning under crosswinds was proposed by Hibino et al. (2010), in which a two-dimensional vehicle model with half of car body, one bogie and two wheelsets was used as shown in Fig. 4. Three degrees of freedom, namely, the rolling angle of car body about axle spring ($\varphi_1$), rolling angle of car body about air spring ($\varphi_2$) and lateral displacement of car body relative to air spring ($y_2$) are adopted to calculate the total displacements of car body, including the lateral displacement ($y_B$), the vertical displacement ($z_B$) and the rolling angle of car body ($\varphi_B$). Total displacements of car body ($y_B$, $z_B$, $\varphi_B$) are shown as:

$$y_B\cong -h_1\varphi_1-h_2\varphi_2+y_2 \tag{10}$$

$$z_B\cong -\frac{1}{2}h_1\varphi_1^2-\frac{1}{2}h_2\varphi_2^2-h_2\varphi_1\varphi_2+y_2\varphi_1 \tag{11}$$

$$\varphi_B\cong\varphi_1+\varphi_2 \tag{12}$$

where $h_1$ is the distance between the center of gravity of car body and the center of axle spring, and $h_2$ is the height between the center of gravity of car body and the center of air spring.

The total displacements of car body ($y_B$, $z_B$, $\varphi_B$) are calculated based on the principle of minimum potential energy considering the vertical stiffness of axis spring, lateral and vertical stiffness of air spring, lateral and vertical stiffness of bump stops. Subsequently, the static equilibrium equation on the wheel-rail contact at the leeward side is expressed as:

$$GP_L=m_Tg\frac{G}{2}+\frac{m_B}{2}g\left(\frac{G}{2}-y_B\right)-F_L\left(\frac{G}{2}-y_B+e\varphi_B\right)-h_{GT}F_u'-h_{GB}(F_u+F_V)-h_{BC}F_S \tag{13}$$

where $G$ is the distance between two wheel-rail contact points. $P_L$ represents the wheel loading on the windward side. $F_L$ and $F_S$ display the lift and side forces caused by crosswinds. $e=h_{BC}-h_{GB}$ exhibits the height between the center of gravity and the wind force center. $h_{BC}$ is the height of wind force center. $h_{GB}$ and $h_{GT}$ are the heights of gravity of car body and bogie, respectively. $F_u=\frac{m_B}{2}\left(\frac{V_{tr}^2}{R}-\frac{c}{G}g\right)$ and $F_u'=m_T\left(\frac{V_{tr}^2}{R}-\frac{c}{G}g\right)$ illustrate the excessive centrifugal forces acting on car body and bogie when a railway vehicle is running on a curve track, and $F_V=\frac{m_B}{2}\frac{V_{tr}}{max\{V_{tr}\}}g$ stands for the lateral force which is caused by the track irregularity. $R$ is the curve radius, and $c$ is the cant, and $g$ is the gravitational acceleration.

The wheel unloading ratio $D$ is derived and expressed as:

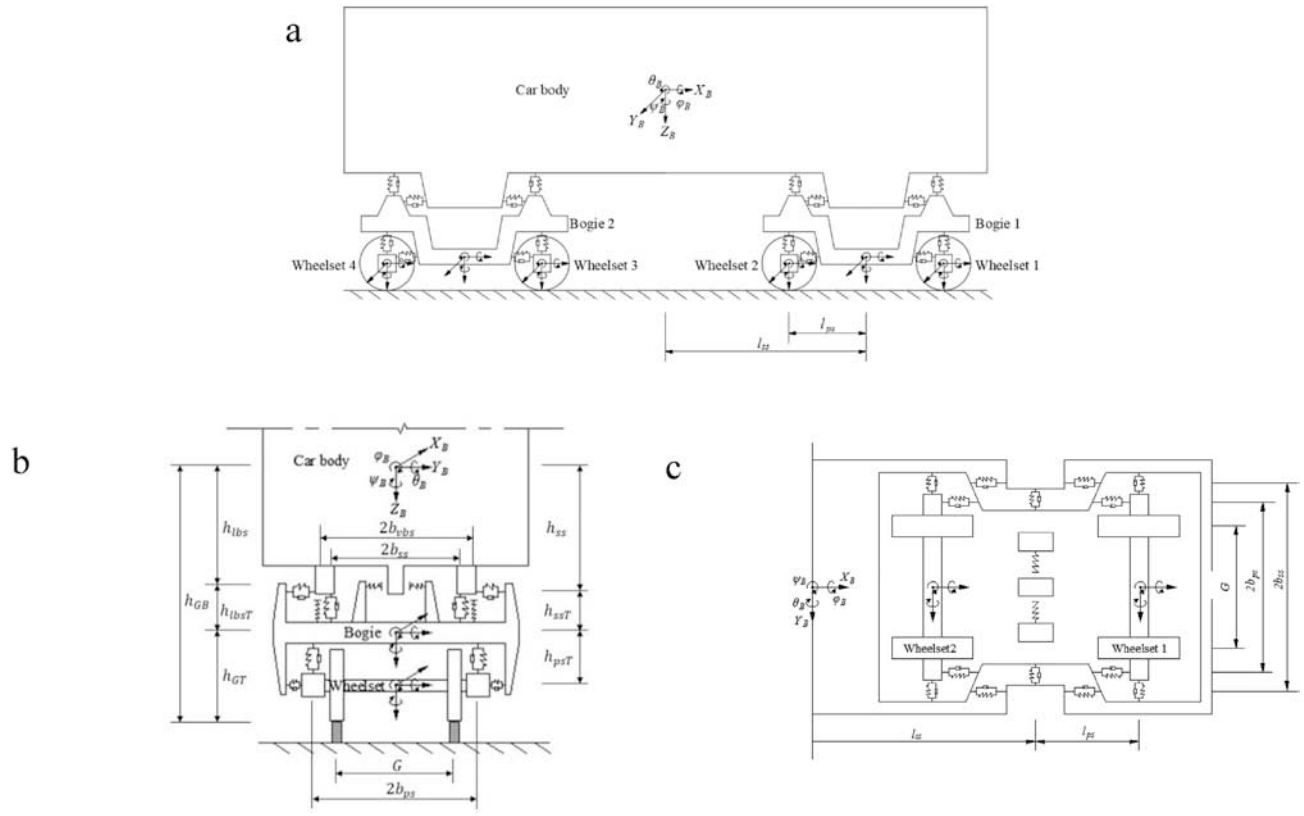


**Fig. 5.** A full vehicle model used in this study: (a) side view; (b) end view; (c) top view.

**Table 1**
Description of degrees of freedom used in the full vehicle model.

| Vehicle body | Longitudinal motion | Lateral motion | Vertical motion | Rolling motion | Pitch motion | Yaw motion |
|---|---|---|---|---|---|---|
| Car body | $X_B$ | $Y_B$ | $Z_B$ | $\phi_B$ | $\theta_B$ | $\psi_B$ |
| Bogie 1 | $X_{T1}$ | $Y_{T1}$ | $Z_{T1}$ | $\phi_{T1}$ | $\theta_{T1}$ | $\psi_{T1}$ |
| Bogie 2 | $X_{T2}$ | $Y_{T2}$ | $Z_{T2}$ | $\phi_{T2}$ | $\theta_{T2}$ | $\psi_{T2}$ |
| Wheelset 1 | $X_{W1}$ | $Y_{W1}$ | $Z_{W1}$ | $\phi_{W1}$ | $\theta_{W1}$ | $\psi_{W1}$ |
| Wheelset 2 | $X_{W2}$ | $Y_{W2}$ | $Z_{W2}$ | $\phi_{W2}$ | $\theta_{W2}$ | $\psi_{W2}$ |
| Wheelset 3 | $X_{W3}$ | $Y_{W3}$ | $Z_{W3}$ | $\phi_{W3}$ | $\theta_{W3}$ | $\psi_{W3}$ |
| Wheelset 4 | $X_{W4}$ | $Y_{W4}$ | $Z_{W4}$ | $\phi_{W4}$ | $\theta_{W4}$ | $\psi_{W4}$ |

$$D = \Delta P \Big/ P_0 = \left(P_0 - P_L\right) \Big/ P_0, \quad P_0 = \frac{(m_B/2 + m_T)g}{2} \tag{14}$$

where $P_0$ represents the static wheel loading and $P_L$ expresses the wheel loading on the windward side as shown in Fig. 4. $\Delta P$ refers to the wheel unloading on the windward side. $m_B$, $m_T$ are the mass of car body and bogie including two wheelsets, respectively.

The unsteady wind effect and the dynamic effect of railway vehicles contribute to the unsteady response. The unsteady wind effect can be expressed by the 3-s averaged wind speed as shown in Appendix B, while the dynamic effect of vehicles cannot be considered in the quasi-static analysis. It is considered by the dynamic amplification factor as proposed in this study.

### 2.3. Multibody dynamic simulations

Multibody dynamic simulations are widely used to predict the dynamic response of railway vehicles with different kinds of external excitations, such as track irregularity, elastic foundation and crosswinds. A full vehicle model as shown in Fig. 5 consists of seven rigid bodies, namely, one car body, two bogies and four wheelsets. Each component has six degrees of freedom, so a whole vehicle has 42 degrees of freedom as described in Table 1. In fact, the number of degrees of freedom for a whole vehicle can be reduced since some displacements are negligible. For example, a vehicle model with 35 degrees of freedom was used by Zhai et al. (2013) and a vehicle model with 31 degrees of freedom was adopted by Hibino et al. (2013b). The primary suspension connecting wheelsets and bogie is simulated by springs and dampers in three directions. Bogies and car body are linked by the secondary suspension system which consists of linear springs and dampers in the vertical, lateral and longitudinal directions. In addition, non-linear bump stops are built in both lateral and vertical directions, respectively. The wheel-rail contact is separated into two parts: the normal contact which provides the normal force and is solved by Hertz theory; and the tangential contact which includes the creep forces in the longitudinal and lateral directions and spin creep torque in the vertical direction and is resolved by Kalker's FASTSIM algorithm (Iwnicki, 2006). Basic parameters including the dimension, mass and moment of inertia of car body, bogies, wheelsets and suspensions are summarized in Table 2 and vehicle suspension forces are described in Table 3. $\Omega$ shows the nominal rolling angular velocity of the wheel and it is related to the train velocity. All these parameters are used in the full vehicle model.

Subsequently, based on D'Alembert's principle, equations of motion of a railway vehicle are built and illustrated as follows:

**Table 2**
Description of basic parameters used in the full vehicle model.

| Notation | Description | Notation | Description |
|---|---|---|---|
| $2b_{ps}$ | lateral distance between two axis springs | $I_{Ty}$ | moment of inertia of bogie about $y$ axis |
| $2b_{ss}$ | lateral distance between two air springs | $I_{Tz}$ | moment of inertia of bogie about $z$ axis |
| $2b_{vbs}$ | lateral distance between two vertical bump stops | $I_{Wx}$ | moment of inertia of wheelset about $x$ axis |
| $G$ | distance between two wheel-rail contact points | $I_{Wy}$ | moment of inertia of wheelset about $y$ axis |
| $h_{ss}$ | height between gravity of car body and air spring | $I_{Wz}$ | moment of inertia of wheelset about $z$ axis |
| $h_{lbs}$ | height between gravity of car body and lateral bump stop | $l_{ps}$ | longitudinal distance between gravity of bogie and air spring |
| $h_{lbsT}$ | height between lateral bump stop and gravity of bogie | $l_{ss}$ | longitudinal distance between gravity car body and gravity of bogie |
| $h_{psT}$ | height between gravity of bogie and axis spring | $m_B$ | mass of car body |
| $h_{ssT}$ | height between air spring and gravity of bogie | $m_T^{'}$ | mass of bogie |
| $I_{Bx}$ | moment of inertia of car body about $x$ axis | $m_W$ | mass of wheelset |
| $I_{By}$ | moment of inertia of car body about $y$ axis | $r_{Li}$ | contact rolling radii of the $i$th wheel on the left side |
| $I_{Bz}$ | moment of inertia of car body about $z$ axis | $r_{Ri}$ | contact rolling radii of the $i$th wheel on the right side |
| $I_{Tx}$ | moment of inertia of bogie about $x$ axis | | |

**Table 3**
Description of vehicle suspension forces used in the full vehicle model.

| Notation | Descriptions | Notation | Descriptions |
|---|---|---|---|
| $F_{Lpskxi}$, $F_{Rpskxi}$ | longitudinal spring forces at primary suspension of the $i$th bogie on left and right sides | $F_{Lssdxi}$, $F_{Rssdxi}$ | longitudinal damping forces at second suspension of the $i$th bogie on left and right sides |
| $F_{Lpskyi}$, $F_{Rpskyi}$ | lateral spring forces at primary suspension of the $i$th bogie on left and right sides | $F_{Lssdyi}$, $F_{Rssdyi}$ | lateral damping forces at second suspension of the $i$th bogie on left and right sides |
| $F_{Lpskzi}$, $F_{Rpskzi}$ | vertical spring forces at primary suspension of the $i$th bogie on left and right sides | $F_{Lssdzi}$, $F_{Rssdzi}$ | vertical damping forces at second suspension of the $i$th bogie on left and right sides |
| $F_{Lpsdxi}$, $F_{Rpsdxi}$ | longitudinal damping forces at primary suspension of the $i$th bogie on left and right sides | $F_{bkyi}$ | spring forces of the lateral bump stop on the $i$th bogie |
| $F_{Lpsdyi}$, $F_{Rpsdyi}$ | lateral damping forces at primary suspension of the $i$th bogie on left and right sides | $F_{Lbkzi}$, $F_{Rbkzi}$ | spring forces of the vertical bump stop on the $i$th bogie on left and right sides |
| $F_{Lpsdzi}$, $F_{Rpsdzi}$ | vertical damping forces at primary suspension of the $i$th bogie on left and right sides | $F_{Lpxi}$, $F_{Lpyi}$ | creep forces of the $i$th wheelset on left side in $x$ and y direction |
| $F_{Lsskxi}$, $F_{Rsskxi}$ | longitudinal spring forces at second suspension of the $i$th bogie on left and right sides | $F_{Rpxi}$, $F_{Rpyi}$ | creep forces of the $i$th wheelset on right side in $x$ and y direction |
| $F_{Lsskyi}$, $F_{Rsskyi}$ | lateral spring forces at second suspension of the $i$th bogie on left and right sides | $M_{Lszi}$, $M_{Rszi}$ | spin creep torque of the $i$th wheelset on left and right side in $z$ direction |
| $F_{Lsskzi}$, $F_{Rsskzi}$ | vertical spring forces at second suspension of the $i$th bogie on left and right sides | $F_{Ltzi}$, $F_{Rtzi}$ | contact forces of the $i$th wheelset on left and right sides in $z$ direction |

Equations of motion of car body ($i$ denotes the number of bogie):

$$\text{Longitudinal motion}\quad m_B\ddot{X}_B = -\sum_{i=1}^{2}(F_{Lsskxi}+F_{Lssdxi}) - \sum_{i=1}^{2}(F_{Rsskxi}+F_{Rssdxi}) \tag{15}$$

$$\text{Lateral motion}\quad m_B\ddot{Y}_B = F_s - \sum_{i=1}^{2}\left(F_{Lsskyi}+F_{Lssdyi}\right) - \sum_{i=1}^{2}\left(F_{Rsskyi}+F_{Rssdyi}\right) - \sum_{i=1}^{2}F_{bkyi} \tag{16}$$

$$\text{Vertical motion}\quad m_B\ddot{Z}_B = -\sum_{i=1}^{2}(F_{Lsskzi}+F_{Lssdzi}) - \sum_{i=1}^{2}(F_{Rsskzi}+F_{Rssdzi}) - \sum_{i=1}^{2}(F_{Lbkzi}+F_{Rbkzi}) + m_Bg - F_L \tag{17}$$

$$\text{Rolling motion}\quad I_{Bx}\ddot{\phi}_B = M + b_{ss}\sum_{i=1}^{2}(F_{Lsskzi}-F_{Rsskzi}) + b_{ss}\sum_{i=1}^{2}(F_{Lssdzi}-F_{Rssdzi}) + b_{vbs}\sum_{i=1}^{2}(F_{Lbkzi}-F_{Rbkzi}) + h_{lbs}\sum_{i=1}^{2}F_{bkyi} + h_{ss}\sum_{i=1}^{2}\left(F_{Lsskyi}+F_{Rsskyi}\right) + h_{ss}\sum_{i=1}^{2}\left(F_{Lssdyi}+F_{Rssdyi}\right) \tag{18}$$

$$\text{Pitch Motion}\quad \begin{aligned} I_{By}\ddot{\theta}_B = {} & (F_{Lsskz1}+F_{Rsskz1}-F_{Lsskz2}-F_{Rsskz2})l_{ss} \\ & +(F_{Lssdz1}+F_{Rssdz1}-F_{Lssdz2}-F_{Rssdz2})l_{ss} \\ & +(F_{Lsskx1}+F_{Rsskx1}+F_{Lsskx2}+F_{Rsskx2})h_{ss} \\ & +(F_{Lssdx1}+F_{Rssdx1}+F_{Lssdx2}+F_{Rssdx2})h_{ss} \\ & +(F_{Lbkz1}+F_{Rbkz1}-F_{Lbkz2}-F_{Rbkz2})l_{ss} \end{aligned} \tag{19}$$

$$\text{Yaw motion}\quad \begin{aligned} I_{Bz}\ddot{\psi}_B = {} & -\left(F_{Lssky1}+F_{Rssky1}-F_{Lssky2}-F_{Rssky2}\right)l_{ss} \\ & -\left(F_{Lssdy1}+F_{Rssdy1}-F_{Lssdy2}-F_{Rssdy2}\right)l_{ss} - \left(F_{bky1}-F_{bky2}\right)l_{ss} \\ & +b_{ss}\sum_{i=1}^{2}(F_{Lsskxi}-F_{Rsskxi}) + b_{ss}\sum_{i=1}^{2}(F_{Lssdxi}-F_{Rssdxi}) \end{aligned} \tag{20}$$

Equations of motion of bogies ($i = 1\tilde{}2$):

$$\text{Longitudinal motion}\quad \begin{aligned} m_T^{'}\ddot{X}_{Ti} = {} & F_{Lsskxi}+F_{Lssdxi}+F_{Rsskxi}+F_{Rssdxi}-F_{Lpsky(2i-1)}-F_{Rpsky(2i-1)} \\ & -F_{Lpsky(2i)}-F_{Rpsky(2i)}-F_{Lpsdy(2i-1)}-F_{Rpsdy(2i-1)}-F_{Lpsdy(2i)} \\ & -F_{Rpsdy(2i)} \end{aligned} \tag{21}$$

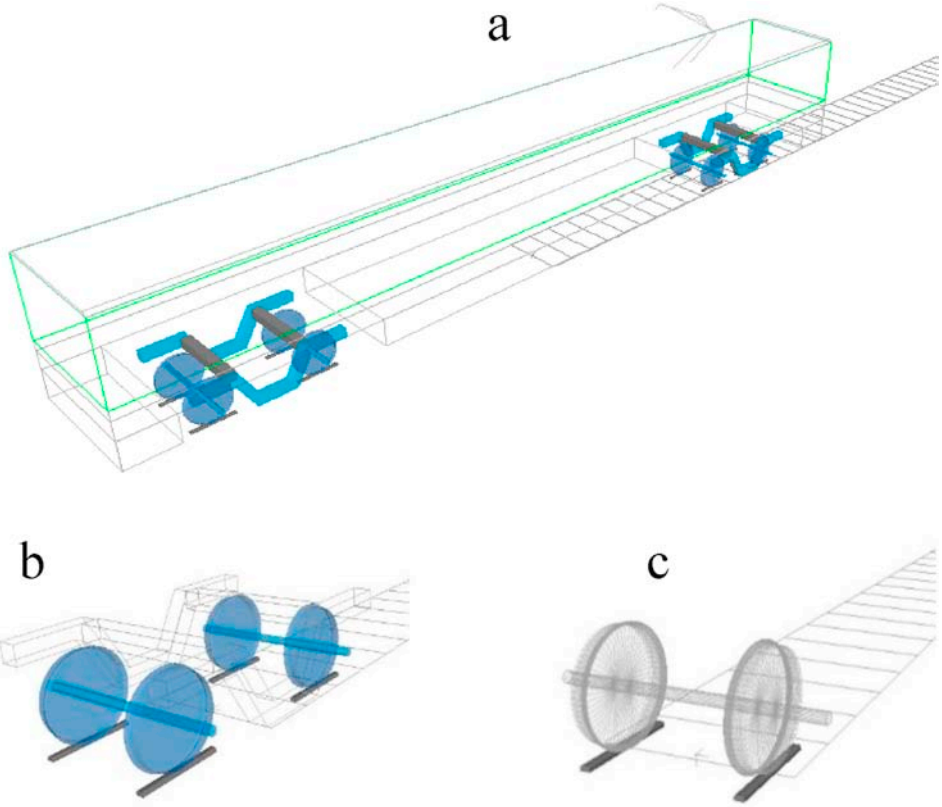


**Fig. 6.** A three-dimensional vehicle model used in multibody dynamic simulations: (a) car body; (b) bogie; (c) wheelset.

Lateral motion

$$\begin{aligned} m_T^{'}\ddot{Y}_{Ti} = {} & F_{Lsskyi} + F_{Lssdyi} + F_{Rsskyi} + F_{Rssdyi} + F_{bkyi} \\ & - F_{Lpsky(2i-1)} - F_{Rpsky(2i-1)} - F_{Lpsky(2i)} - F_{Rpsky(2i)} - F_{Lpsdy(2i-1)} - F_{Rpsdy(2i-1)} \\ & - F_{Lpsdy(2i)} - F_{Rpsdy(2i)} \end{aligned} \tag{22}$$

Vertical motion

$$\begin{aligned} m_T^{'}\ddot{Z}_{Ti} = {} & F_{Lsskzi} + F_{Lssdzi} + F_{Rsskzi} + F_{Rssdzi} + F_{Lbkzi} + F_{Rbkzi} - F_{Lpskz(2i-1)} \\ & - F_{Rpskz(2i-1)} - F_{Lpsdz(2i-1)} - F_{Rpsdz(2i-1)} - F_{Lpskz(2i)} - F_{Rpskz(2i)} \\ & - F_{Lpsdz(2i)} - F_{Rpsdz(2i)} + m_T^{'}g \end{aligned} \tag{23}$$

Rolling motion

$$\begin{aligned} I_{Tx}\ddot{\phi}_{Ti} = {} & b_{ss}(F_{Rsskzi} - F_{Lsskzi}) + b_{ss}(F_{Rssdzi} - F_{Lssdzi}) + b_{vbs}(F_{Rbkzi} - F_{Lbkzi}) \\ & + h_{lbsT}F_{bkyi} \\ & + h_{ssT}\left(F_{Lsskyi(2i-1)} + F_{Rsskyi(2i-1)} + F_{Lsskyi(2i)} + F_{Rsskyi(2i)}\right) \\ & + h_{ssT}\left(F_{Lssdyi(2i-1)} + F_{Rssdyi(2i-1)} + F_{Lssdyi(2i)} + F_{Rssdyi(2i)}\right) \\ & + h_{psT}\left(F_{Lpsky(2i-1)} + F_{Rpsky(2i-1)} + F_{Lpsky(2i)} + F_{Rpsky(2i)}\right) \\ & + h_{psT}\left(F_{Lpsdy(2i-1)} + F_{Rpsdy(2i-1)} + F_{Lpsdy(2i)} + F_{Rpsdy(2i)}\right) \\ & + b_{ps}\left(F_{Lpskz(2i-1)} + F_{Lpskz(2i)} - F_{Rpskz(2i-1)} - F_{Rpskz(2i)}\right) \\ & + b_{ps}\left(F_{Lpsdz(2i-1)} + F_{Lpsdz(2i)} - F_{Rpsdz(2i-1)} - F_{Rpsdz(2i)}\right) \end{aligned} \tag{24}$$

Pitch motion

$$\begin{aligned} I_{Ty}\ddot{\theta}_{Ti} = {} & h_{ssT}(F_{Rsskxi} + F_{Lsskxi} + F_{Rssdxi} + F_{Lssdxi}) \\ & + l_{ps}\left(F_{Lpskz(2i-1)} + F_{Rpskz(2i-1)} - F_{Lpskz(2i)} - F_{Rpskz(2i)}\right) \\ & + l_{ps}\left(F_{Lpsdz(2i-1)} + F_{Rpsdz(2i-1)} - F_{Lpsdz(2i)} - F_{Rpsdz(2i)}\right) \\ & + h_{psT}\left(F_{Lpskx(2i-1)} + F_{Rpskx(2i-1)} + F_{Lpskx(2i)} + F_{Rpskx(2i)}\right) \\ & + h_{psT}\left(F_{Lpsdx(2i-1)} + F_{Rpsdx(2i-1)} + F_{Lpsdx(2i)} + F_{Rpsdx(2i)}\right) \end{aligned} \tag{25}$$

Yaw motion

$$\begin{aligned} I_{Tz}\ddot{\psi}_{Ti} = {} & -b_{ss}(F_{Lsskxi} - F_{Rsskxi}) - b_{ss}(F_{Lssdxi} - F_{Rssdxi}) \\ & - l_{ps}\left(F_{Lpsky(2i-1)} + F_{Rpsky(2i-1)} - F_{Lpsky(2i)} - F_{Rpsky(2i)}\right) \\ & - l_{ps}\left(F_{Lpsdy(2i-1)} + F_{Rpsdy(2i-1)} - F_{Lpsdy(2i)} - F_{Rpsdy(2i)}\right) \\ & + b_{ps}\left(F_{Lpskx(2i-1)} + F_{Lpskx(2i)} - F_{Rpskx(2i-1)} - F_{Rpskx(2i)}\right) \\ & + b_{ps}\left(F_{Lpsdx(2i-1)} + F_{Lpsdx(2i)} - F_{Rpsdx(2i-1)} - F_{Rpsdx(2i)}\right) \end{aligned} \tag{26}$$

**Table 4**
Description of basic settings used in SIMPACK.

| Items | Explanation |
|---|---|
| Wheel profile | S1002 |
| Rail profile | UIC 60 |
| Wheel/rail contact | Kalker's FASTSIM |
| Iteration method | SODASRT 2 |

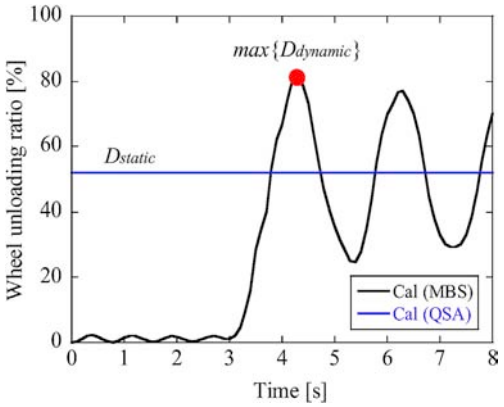


**Fig. 7.** The maximum dynamic and static wheel unloading ratio.

Equations of motion of wheelsets $(i = 1\tilde{}4)$ :

Longitudinal motion $$m_W\ddot{X}_{Wi} = -F_{Lpxi} - F_{Rpxi} + F_{Lpskxi} + F_{Rpskxi} + F_{Lpsdxi} + F_{Rpsdxi} \tag{27}$$

Lateral motion $$m_W\ddot{Y}_{Wi} = -F_{Lpyi} - F_{Rpyi} + F_{Lpskyi} + F_{Rpskyi} + F_{Lpsdyi} + F_{Rpsdyi} \tag{28}$$

Vertical motion $$m_W\ddot{Z}_{Wi} = -F_{Ltzi} - F_{Rtzi} + F_{Lpskzi} + F_{Rpskzi} + F_{Lpsdzi} + F_{Rpsdzi} + m_W g \tag{29}$$

Rolling motion
$$\begin{aligned} & I_{Wx}\ddot{\phi}_{Wi} - \left(I_{Wy} - I_{Wz}\right)\left(\dot{\theta}_{Wi} - \Omega\right)\dot{\psi}_{Wi} \\ & = \frac{G}{2}\left(F_{Ltzi} - F_{Rtzi}\right) + \left(r_{Li}F_{Lpyi} + r_{Ri}F_{Rpyi}\right) + b_{ps}\left(F_{Rpskzi} - F_{Lpskzi}\right) \\ & + b_{ps}\left(F_{Rpsdzi} - F_{Lpsdzi}\right) \end{aligned} \tag{30}$$

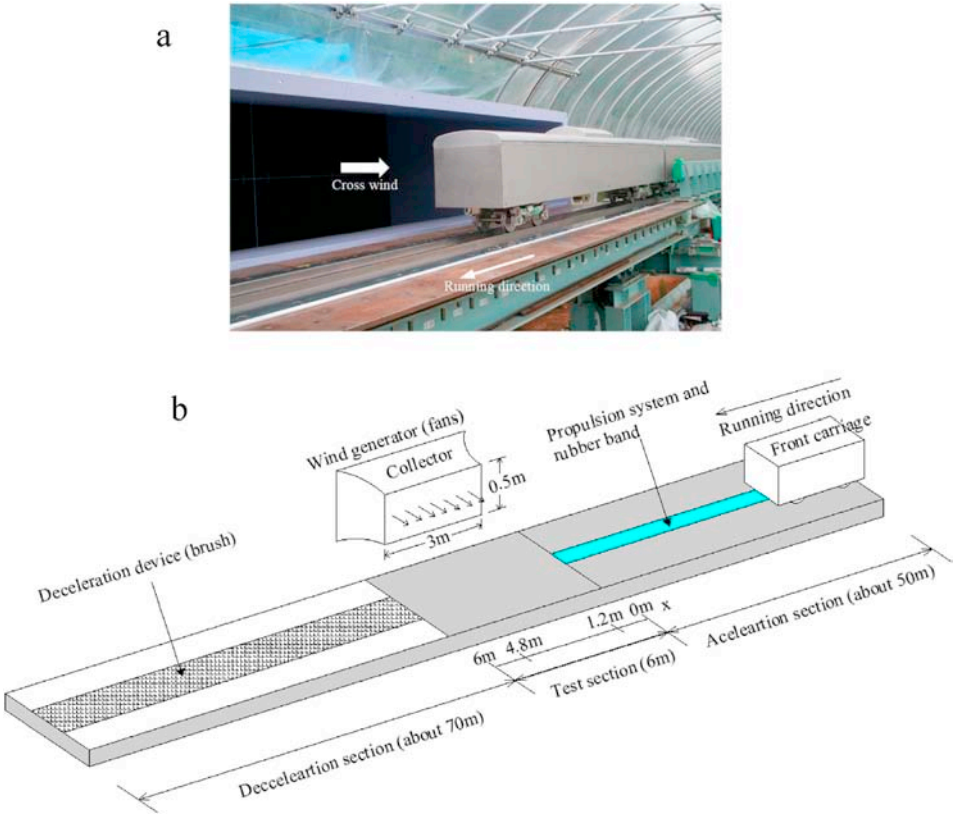


**Fig. 8.** Scale model vehicle and running vehicle test: (a) photo of scale model vehicle; (b) overview of running vehicle test.

**Table 5**
Description of typical structural parameters of the model vehicle.

| Notation | Value | Unit | Notation | Value | Unit |
|---|---|---|---|---|---|
| $A$ | 0.513 | $m^2$ | $h_{GT}$ | 0.055 | $m$ |
| $G$ | 0.112 | $m$ | $H_0$ | 0.263 | $m$ |
| $h_1$ | 0.171 | $m$ | $L_0$ | 1.95 | $m$ |
| $h_2$ | 0.125 | $m$ | $m_B$ | 14.64 | $kg$ |
| $h_{GB}$ | 0.214 | $m$ | $m_T$ | 5.295 | $kg$ |

Pitch Motion
$$I_{Wy}\ddot{\theta}_{Wi} = r_{Li}F_{Lpxi} + r_{Ri}F_{Rpxi} + \left(r_{Li}\psi_{Wi}F_{Lpyi} + r_{Ri}\psi_{Wi}F_{Rpyi}\right) \quad (31)$$

Yaw Motion
$$I_{Wz}\ddot{\psi}_{wi} - \left(I_{Wx} - I_{Wy}\right)\left(\dot{\theta}_{Wi} - \Omega\right)\dot{\phi}_{Wi} = \frac{G}{2}\left(F_{Lpxi} - F_{Rpxi}\right) + \frac{G}{2}\psi_{wi}\left(F_{Lpyi} - F_{Rpyi}\right) + \left(M_{Lszi} + M_{Rszi}\right) - b_{ps}\left(F_{Lpskxi} - F_{Rpskxi}\right) - b_{ps}\left(F_{Lpsdxi} - F_{Rpsdxi}\right) \quad (32)$$

The basic parameters which are used in the above equations of motion, including the mass and moment of inertia of car body, bogies, wheelsets are described in Table 2. The geometric parameters, including the longitudinal, lateral and vertical distances of suspension forces, are shown in Table 2 and drawn in Fig. 5. The suspension forces in the primary and second suspension systems are listed in Table 3.

The equations of motion for the 42 degrees of freedom vehicle model are solved by the commercial code SIMPACK 2017.1 (Dassault Systems, 2017). The corresponding railway vehicle model is shown in Fig. 6. Wheel and rail profiles as well as algorithms used in SIMPACK are listed in Table 4.

Three displacements of car body ($y_B, z_B, \varphi_B$) shown in Eqs. (10) (11) and (12) are approximated, and displacements of bogies are neglected in the quasi-static analysis, while they are considered in multibody dynamic simulations. The lateral displacements of car body calculated by both methods will be compared and discussed in section 3.3. Furthermore, all damping parameters are ignored in the quasi-static analysis and these are also considered in multibody dynamic simulations. The dynamic amplification factor defined below will be significantly affected by the damping parameters and it will be explained in section 3.3. Finally, the inertial forces are neglected in the quasi-static analysis which means the dynamic effect cannot be included. The quasi-static analysis can calculate wheel unloading ratio at any steady winds, but it cannot directly evaluate the dynamic response of railway vehicles under unsteady wind speeds which means time-series wind excitations cannot be taken into account. However, the quasi-static analysis has been widely used to assess the crosswind stability of the commuter rail, since it is convenient to calculate the characteristic wind curve compared with multibody dynamic simulations. Multibody dynamic simulations need series of calculations to obtain the critical situation of vehicle overturning at one train velocity, thus it is time-consuming and with great computational work (Carrarini, 2008).

### 2.4. Dynamic amplification factor

The dynamic amplification factor (DAF) has been used in the structure engineering and defined as the maximum dynamic load divided by the maximum static load effect (Brady and O'Brien, 2006). In order to evaluate the crosswind stability of railway vehicles, the wheel unloading ratio which describes a certain proportion of wheel unloading is adopted. The maximum dynamic wheel unloading ratio is calculated by multibody dynamic simulations (MBS), while static wheel unloading ratio is obtained by the quasi-static analysis (QSA) as shown in Fig. 7. The dynamic amplification factor (DAF) defined as the maximum dynamic wheel unloading ratio divided by the static wheel unloading ratio is written as:

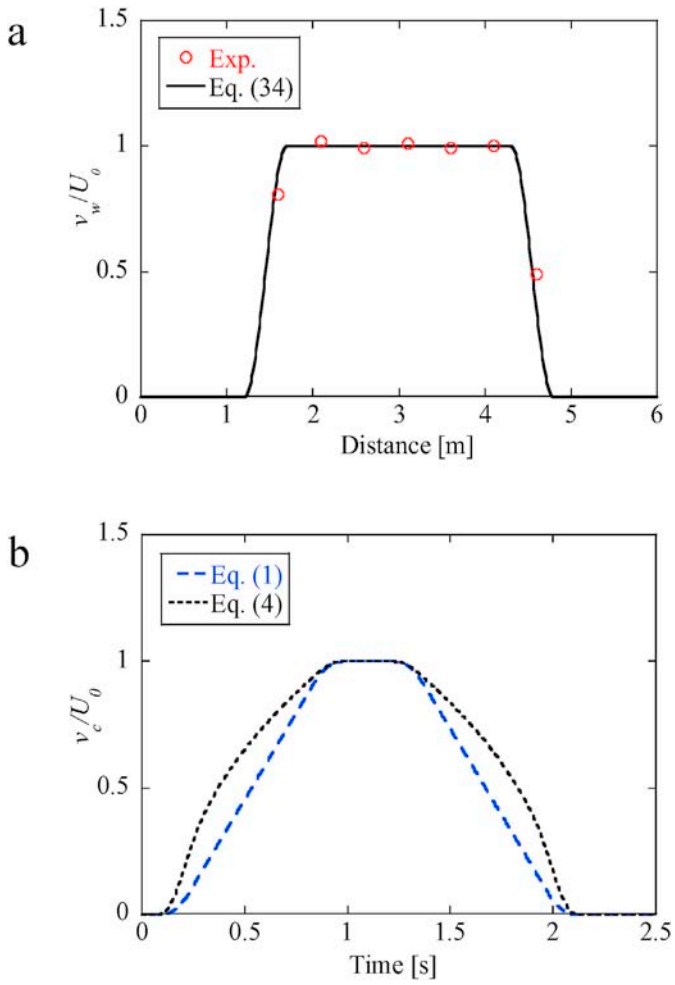


**Fig. 9.** Wind distributions in the test section: (a) in space domain; (b) in time domain.

$$DAF = \frac{max\{D_{dynamic}\}}{D_{static}} \quad (33)$$

where $D_{dynamic}$, $D_{static}$ represent the dynamic and static wheel unloading ratio, respectively.

## 3. Dynamic response of railway vehicles

Dynamic responses of a model vehicle and a commuter rail are investigated by multibody dynamic simulations and compared with the experimental data in section 3.1 and section 3.2, respectively. The dynamic amplification factor of the railway vehicle under tunnel exit winds is systematically studied and a simple formula is proposed to predict the DAF in section 3.3.

### 3.1. Dynamic response of a model vehicle

A model vehicle built by Hibino et al. (2013a) is used to investigate the modelling of aerodynamic forces and the dynamic response of railway vehicles under tunnel exit winds as shown in Fig. 8(a). The scale of the model vehicle is 1/10 based on the 103 series introduced by Japanese National Railways. The model vehicle is fabricated to satisfy the geometric and mechanical similarities. The spring constant of model vehicles including first and second suspension is 1/100 times as stiff as the prototype vehicle and the mass for each component including car body,

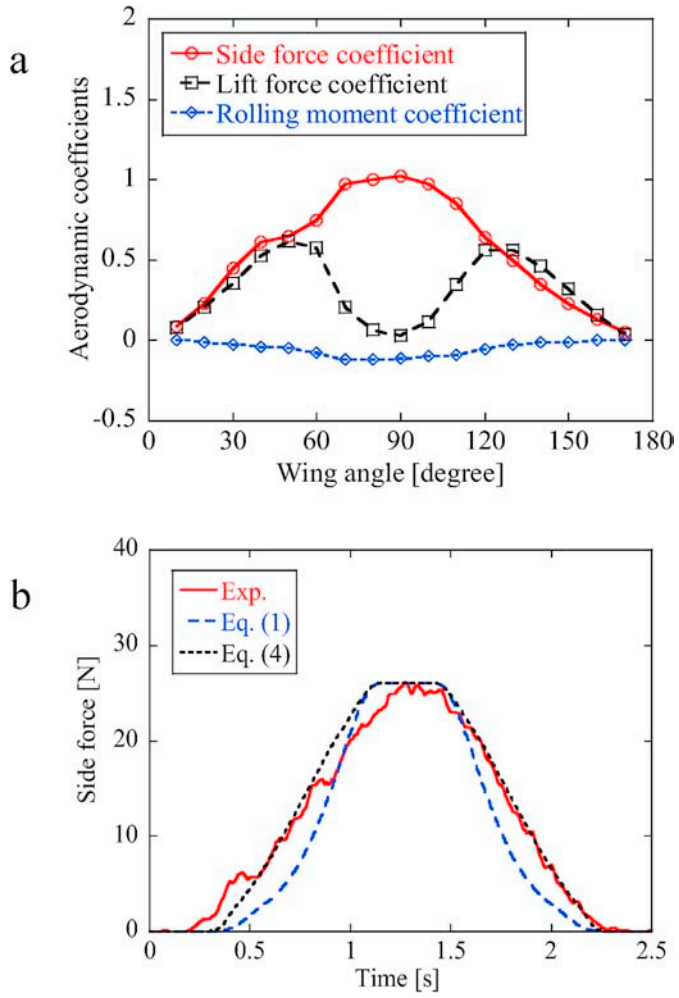


**Fig. 10.** Comparisons of (a) aerodynamic coefficients of the model vehicle and (b) side forces acting on the model vehicle.

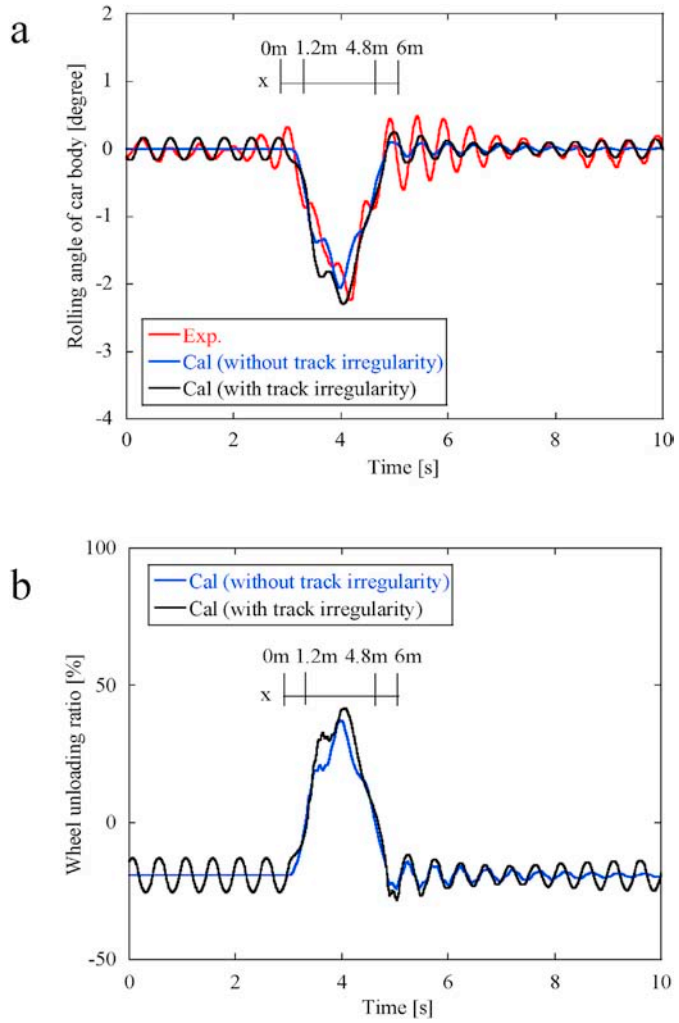


**Fig. 11.** Dynamic responses of the model vehicle: (a) rolling angle of car body; (b) wheel unloading ratio.

bogie and wheelset is 1/1000 times as heavy as the prototype one. It means that the natural frequency of the vehicle model is 3.162 times higher than that of vehicle in full scale. The typical structural parameters of the model vehicle are presented in Table 5 which are used in the quasi-static analysis. The running vehicle tests using the model vehicle were carried out by Hibino et al. (2013a).

The natural frequency of roll motion in full scale is estimated by eigenvalue analyses and is shown in Table A1. The natural frequency of roll motion obtained by eigenvalue analysis in the wind tunnel test is 0.500 Hz in full scale and is 1.111 times higher than the natural frequency of 0.451 Hz for the commuter rail as shown in Table 8 since the four additional springs in the vertical direction are used in the vehicle model. The effect of the natural frequency of the vehicle model on DAF is systematically studied in Section 3.3.

The experimental equipment can be separated into three sections, that is, the acceleration section, the test section and the deceleration section as shown in Fig. 8(b), where only the front carriage of model vehicle is drawn. The model vehicle is accelerated by the propulsion system and there is no crosswind in the acceleration section. The railway vehicle running in the tunnel is simulated in this section. The model vehicle then enters the test section where a collector is installed to smoothly accelerate airflow generated by fans. The side area of the front carriage subjected to crosswinds increases gradually when the model vehicle runs forward at a constant velocity until the whole front carriage is attacked by the uniform flow from the collector. This condition is the same as that a railway vehicle is running out of a tunnel and is attacked by crosswinds. In the test section, the train velocity is $V_{tr} = 9.8km/h$, and the wind speed is $U_0 = 8.8m/s$. At last, the model vehicle drives into the deceleration section and decelerates by brush. It simulates a railway vehicle running into another tunnel again. The length of the collector is 3 $m$ which is longer than the 2 $m$ length of the front carriage, thus the whole carriage can be subjected to the crosswind before it moves into another tunnel.

**Table 6**
Maximum rolling angle of car body and relative error.

| Case | Maximum rolling angle [degree] | Relative error [%] |
|---|---|---|
| Experiment | 2.25 | – |
| Simulation without track irregularity | 2.07 | −8.0 |
| Simulation with track irregularity | 2.30 | 2.2 |

Aerodynamic forces and the dynamic response of model vehicles against tunnel exit winds were measured as shown in Hibino et al. (2013a). The pressures on the car body surface were measured by pressure taps and aerodynamic forces acting on the model vehicle were calculated by integration of surface pressures. The dynamic response of the model vehicle is obtained by an inertial measurement equipment placed in the car body. In general, the wheel unloading ratio is used to

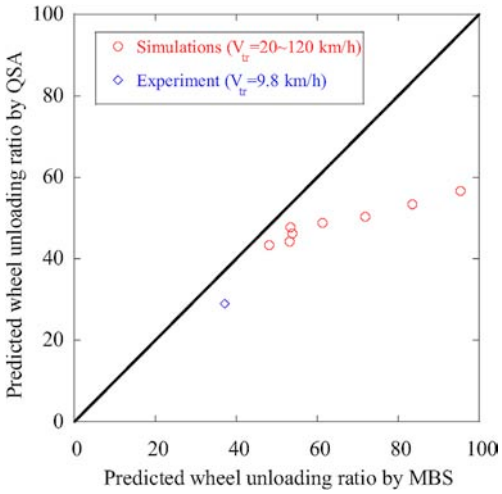


**Fig. 12.** Comparisons of wheel unloading ratios predicted by the quasi-static analysis and multibody dynamic simulations.

evaluate the dynamic response of railway vehicles. However, there are some limitations to measure time series data of wheel loading for a moving railway vehicle, thus the rolling angle of car body is regarded as an alternative indicator to show the dynamic behavior of railway vehicles against crosswinds.

Aerodynamic forces are calculated by two different methods, one is the centered moving average method as shown in Eq. (1) and the other is the equivalent wind force method proposed in section 2.1 as written in Eq. (4) and compared with the experimental data. For the running vehicle test, the wind distribution in the test section can be defined as Eq. (34).

$$v_w = \begin{cases} \frac{1}{2}U_0\left[1 - cos\frac{2\pi(1.8+x)}{2L}\right] & 1.2 \le x < 1.7 \\ U_0 \quad 1.7 \le x < 4.3 \\ \frac{1}{2}U_0\left[1 - cos\frac{2\pi(1.8-x)}{2L}\right] & 4.3 \le x < 4.8 \end{cases} \tag{34}$$

where $U_0$ is the gust amplitude and refers to the maximum wind speed, $L$ is the gust duration and describes how long the wind speed increases from zero to the maximum value in space domain as shown in Fig. 2. $x$ shows distance as illustrated in Fig. 8. The gust duration $L$ expresses the effect of surface roughness of the mountain and can be evaluated by the wind distribution using the numerical simulations. The surface roughness of the mountain was not introduced in the wind tunnel test for simplification. The effect of gust duration $L$ is systematically investigated in Section 3.3.

The wind speed at the central part of the collector is expressed as a constant velocity $U_0 = 8.8m/s$, and the wind speeds at the two sides decreases to zero at the boundary of collector. One-minus-cosine gust model is used to simulate the wind speed at the two sides. The gust duration $L$ is assumed to be 0.5 $m$. The predicted wind distribution as illustrated in Fig. 9(a) shows good agreement with measurement data by Hibino et al. (2011a) The temporal wind speed at the vehicle center which is low-pass filtered by the centered moving average method and the equivalent wind force method are shown in Fig. 9(b), respectively. It is obvious that the wind speed at the vehicle center is underestimated when the centered moving averaged method in Eq. (1) is used.

As shown in Fig. 10(a), aerodynamic coefficients of the model vehicle have been measured by wind tunnel test (Hibino et al., 2013a) in which the model vehicle was placed on ground and the uniform wind was adopted. The side forces acting on the model vehicle calculated by two different methods are compared with the experiment as illustrated in Fig. 10(b). The side force obtained by the equivalent wind force method

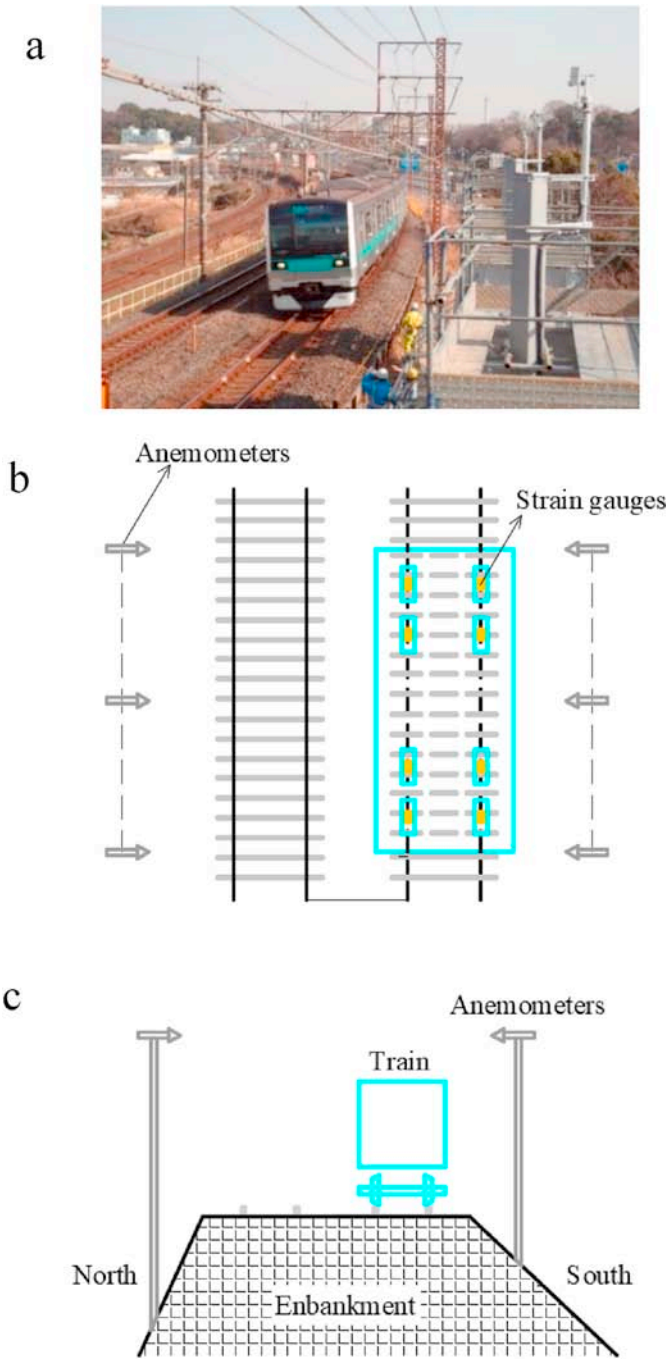


**Fig. 13.** Description of the commuter rail and field test: (a) photo of the commuter rail; (b) top view; (c) front view.

as written in Eq. (4) matches well with the experimental data, while those calculated by the centered moving average method as shown in Eq. (1) are significantly underestimated comparing with the experiment. Some discrepancies between the side force predicted by the equivalent wind force method are observed due to the interaction between the crosswind and the moving vehicle. The effect of the discrepancies of side force on the dynamic response of the vehicles are discussed below.

The dynamic response of the model vehicle under tunnel exit winds was measured using the inertial measurement device by Hibino et al. (2013a). The identified parameters shown in Appendix A are used in this study. Fig. 11(a) shows the rolling angle of car body obtained by multibody dynamic simulations. The maximum rolling angle of car body calculated by the equivalent wind force method is slightly smaller than

that obtained by experiment since the track irregularity may increase the vibration of car body. In order to investigate the effect of track irregularity on the rolling angle of car body, the sinusoidal lateral force which is identified by the experimental data in Appendix A is applied to simulate effect of the track irregularity. It is found the maximum rolling angle of car body considering the track irregularity can be improved and it is favorably close to experiment data. The relative errors of maximum rolling angle is −8% when aerodynamic forces calculated by the equivalent wind force method and it decreases to 2.2% for the cases with the track irregularity as shown in Table 6. The rolling angles of car body at the beginning and end sections show good agreement with the experimental data, which implies that the effect of track irregularity is reproduced as well. In addition, Fig. 11(b) shows wheel unloading ratios with and without considering track irregularity. Similar to the rolling angle of car body, the maximum dynamic responses of the vehicle model increase slightly if the track irregularity is added. It is found that the tunnel exit wind can be predicted by the one-minus-cosine gust model and aerodynamic forces can be calculated by the equivalent wind force method and quasi-steady theory. Afterwards the dynamic response of railway vehicles under tunnel exit winds can be evaluated by multibody dynamic simulations.

In addition, Fig. 12 shows comparisons of wheel unloading ratios calculated by both quasi-static analysis and multibody dynamic simulations in which the blue point represents the experiment case with the train velocity of $V_{tr} = 9.8km/h$, and red points stand for the cases when the train velocity increases from $10km/h$ to $80km/h$ at the interval of $10km/h$. The gust amplitude maintains $U_0 = 8.8m/s$ for all cases as same as that used in the experiment. It is found that the wheel unloading ratios are obviously underestimated by the quasi-static analysis as the train velocity increases.

### 3.2. Dynamic response of a commuter rail

In order to investigate the dynamic response of a commuter rail under natural winds, field tests were carried out by East Japan Railway Company in Japan, and the E233 series commuter rail was used as shown in Fig. 13(a), which is operated extensively in Tokyo Megalopolis. The railway substructure is an embankment and the test section is a curve track, in which the curve radius $R$ is 600 $m$ and the cant $c$ is 85 $mm$. Eight strain gauges were installed on the tracks at a constant distance to make sure that the wheel loading of each wheel could be measured at the same time when the commuter rail passed through them. The wind speeds were simultaneously measured by anemometers which were laid on the two sides of the track, and the crosswind blew from both sides can be measured. The schematic of field test is presented in Fig. 13(b) and (c). It draws on a tangent track for the sake of simplicity.

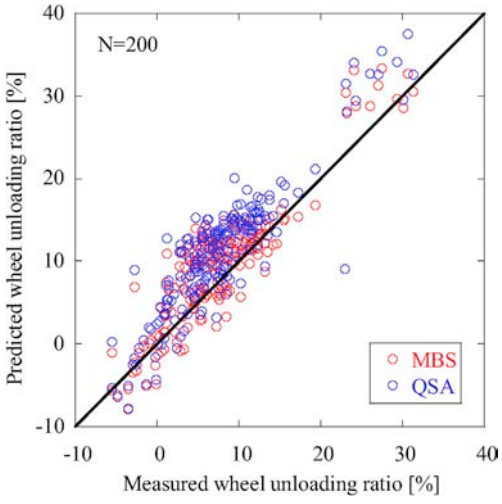


**Fig. 14.** Comparisons of wheel unloading ratio obtained by measurements and predictions.

In the multibody dynamic simulations, the 3-s average wind speed method proposed by Nagumo and Ishihara (2020) is used to consider the spatial correlation of wind speed along the whole carriage as shown in Appendix B. The wind speed was measured at about 5 $m$ height, which was slightly higher than the vehicle center. Therefore, the wind speed is multiplied by a factor of 0.8 obtained from the wind tunnel test as shown in Imai et al., (2002) and Hibino et al., (2011b). In addition, aerodynamic coefficients for the southerly wind were measured from the wind tunnel test. On the other hand, aerodynamic coefficients for the northerly wind are multiplied by a factor of 0.7 since the substructure is different, which was also obtained from the wind tunnel test. The excessive centrifugal forces acting on the car body $F_u$ and the bogie $F_u'$ are added to simulate the curve track.

Fig. 14 presents the predicted wheel unloading ratios by both quasi-static analysis (Nagumo and Ishihara, 2020) and multibody dynamic simulations and the measured values. The total number is 200. The predicted wheel unloading ratios by both quasi-static analysis and multibody dynamic simulations show favorably agreement with the experimental data. The variations between numerical results and experimental data are mainly caused by the uncertainty of track irregularity. Furthermore, the average wheel unloading ratio obtained from multibody dynamic simulations is about 2% larger than the experimental data while it is about 3% for the quasi-static analysis. Therefore, it is concluded that wheel unloading ratios calculated by both methods are extremely the same when railway vehicles are attacked by natural winds. As for the 2% or 3% error, it may be caused by the cant of the railway track, which has a great influence on the excessive centrifugal forces acting on the railway vehicle.

### 3.3. Dynamic amplification factor for railway vehicles

The dynamic amplification factor for railway vehicles in the tunnel exit winds is investigated in this section and only the operational commuter rail (E233 series) is considered. The tunnel exit wind has been illustrated in section 2.1, and there are two essential factors, including gust duration $L$ and gust amplitude $U_0$. The gust duration $L$ shows how long the wind speed increases from zero to the gust amplitude $U_0$, and it can be decided by the shape of the tunnel exit. When the wind speed increases gradually, gust duration $L$ may have a large value, for example 40 $m$ (twice the carriage length). On the contrary, gust duration $L$ may be assumed as 5 $m$ ($1/4th$ the carriage length) as the wind speed increases sharply. As for gust amplitude $U_0$, it changes from 5 $m/s$ to 20 $m/s$. Ten cases are studied and train velocity $V_{tr}$ increases from 20 $km/h$ to 120 $km/h$ at the interval of 20 $km/h$ in all cases, as shown in Table 7. The wind speeds at the vehicle center are low-pass filtered by the equivalent wind force method and they change with the gust duration and the gust amplitude in Fig. 15.

Aerodynamic forces are calculated by the quasi-steady theory and they are shown in Fig. 16. The side force and rolling moment change from zero and increase to the maximum value gradually while the lift force

**Table 7**
Description of simulation cases and the tunnel exit wind parameters.

| Case | $L$ [m] | $U_0$ [$m/s$] | $V_{tr}$ [$km/h$] |
|---|---|---|---|
| 1 | 5 | 10 | 20–120 at the interval of 20 |
| 2 | 5 | 20 | 20–120 at the interval of 20 |
| 3 | 10 | 10 | 20–120 at the interval of 20 |
| 4 | 10 | 20 | 20–120 at the interval of 20 |
| 5 | 20 | 5 | 20–120 at the interval of 20 |
| 6 | 20 | 10 | 20–120 at the interval of 20 |
| 7 | 20 | 15 | 20–120 at the interval of 20 |
| 8 | 20 | 20 | 20–120 at the interval of 20 |
| 9 | 40 | 10 | 20–120 at the interval of 20 |
| 10 | 40 | 20 | 20–120 at the interval of 20 |

changes from a none zero value and it means it is existed even if the angle of attack for wind is zero.

The dynamic responses of the commuter rail under tunnel exit winds are calculated by multibody dynamic simulations and quasi-static analysis in Fig. 17 and in Fig. 18, respectively. It is noted that all dynamic responses increase as the tunnel exit winds increase and then oscillate, and finally tend to be constant values. The dynamic responses will still rise even if the tunnel exit winds have already changed to be constant, therefore, the maximum dynamic responses are larger than the final constant values and this is the dynamic amplification effect caused by tunnel exit winds. It is also found that lateral displacements of car body calculated by quasi-static analysis is slightly smaller than that obtained by multibody dynamic simulations in Fig. 17. This is because the lateral displacements of car body are approximated in the quasi-static analysis and they may cause some errors. However, wheel unloading ratios

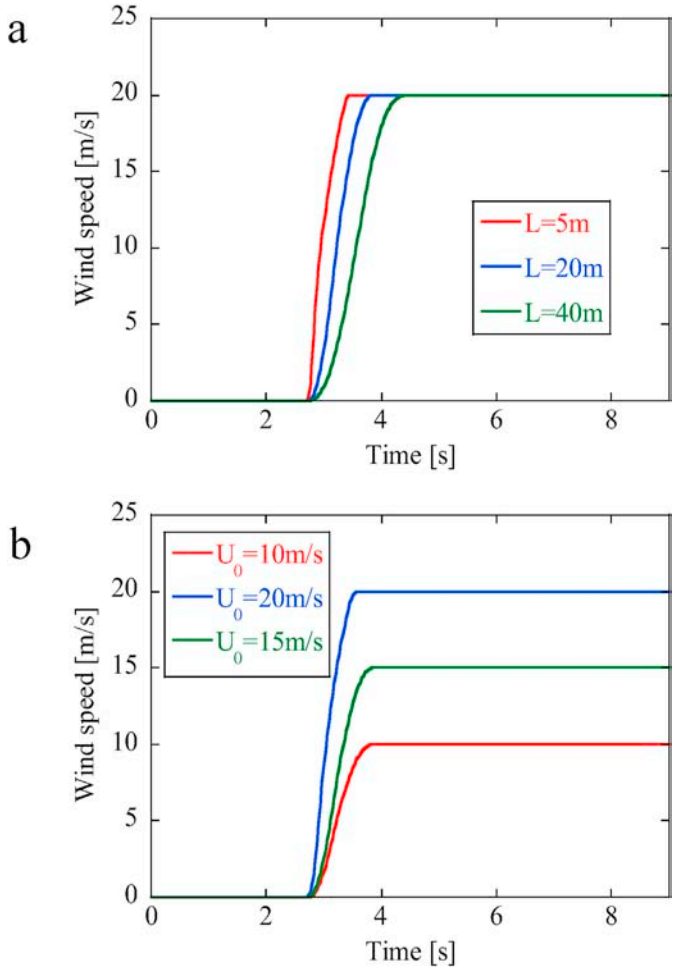


**Fig. 15.** Variations of tunnel exit winds at vehicle center in time domain ($V_{tr}$ = 120$km/h$): (a) with gust duration; (b) with gust amplitude.

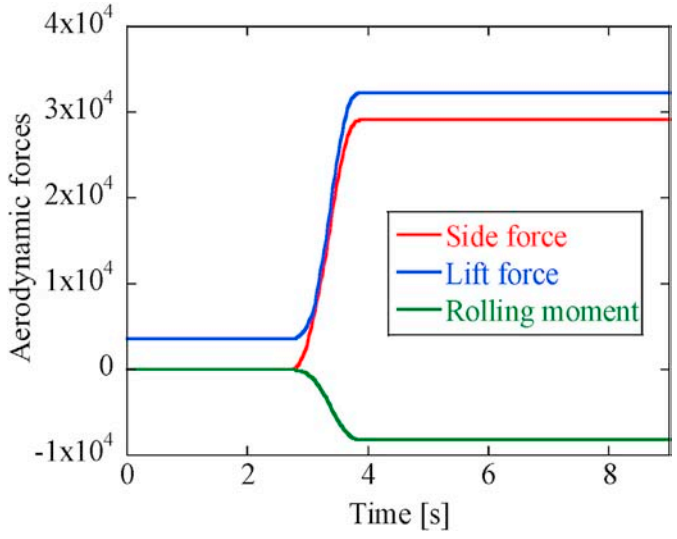


**Fig. 16.** Aerodynamic forces caused by tunnel exit winds ($U_0$ = 20$m/s$, $L$ = 20$m$, $V_{tr}$ = 120$km/h$).

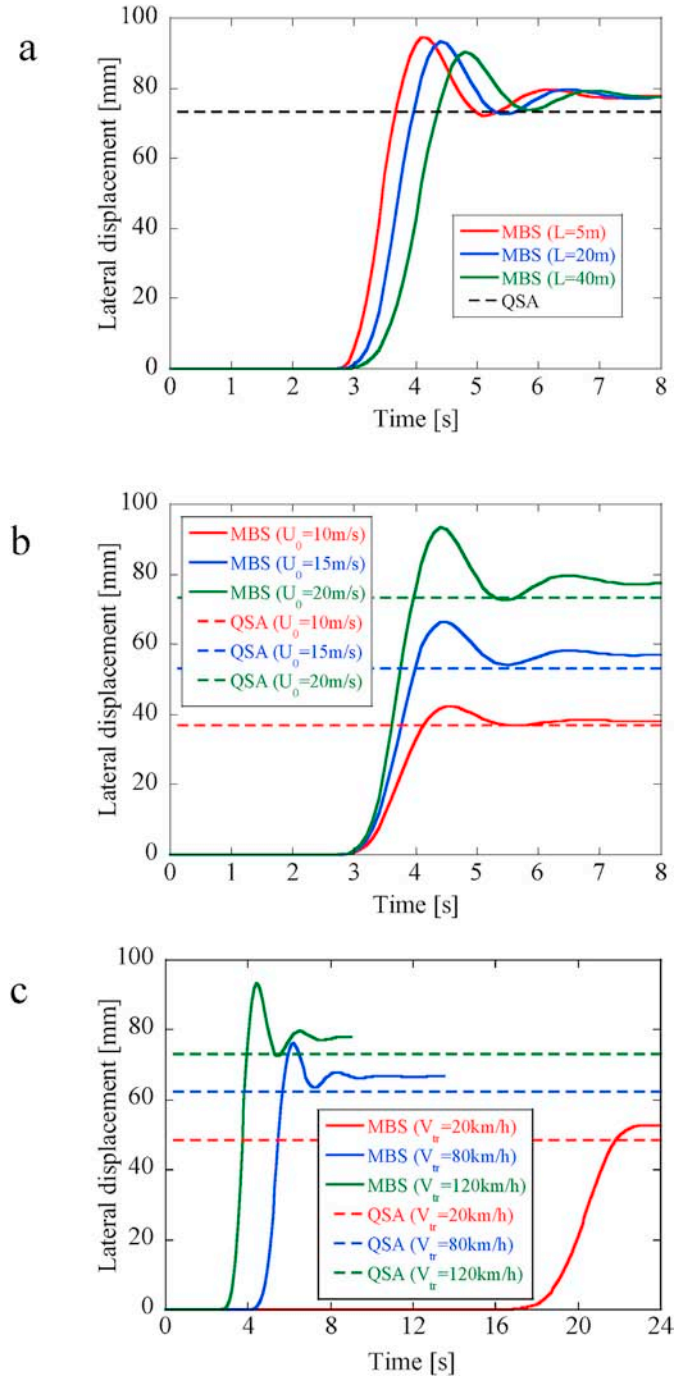


**Fig. 17.** Variations of lateral displacement of center of gravity of car body with: (a) gust duration ($U_0$ = 20$m/s$, $V_{tr}$ = 120$km/h$); (b) gust amplitude ($L$ = 20$m$, $V_{tr}$ = 120$km/h$); (c) train velocity ($L$ = 20$m$, $U_0$ = 20$m/s$)

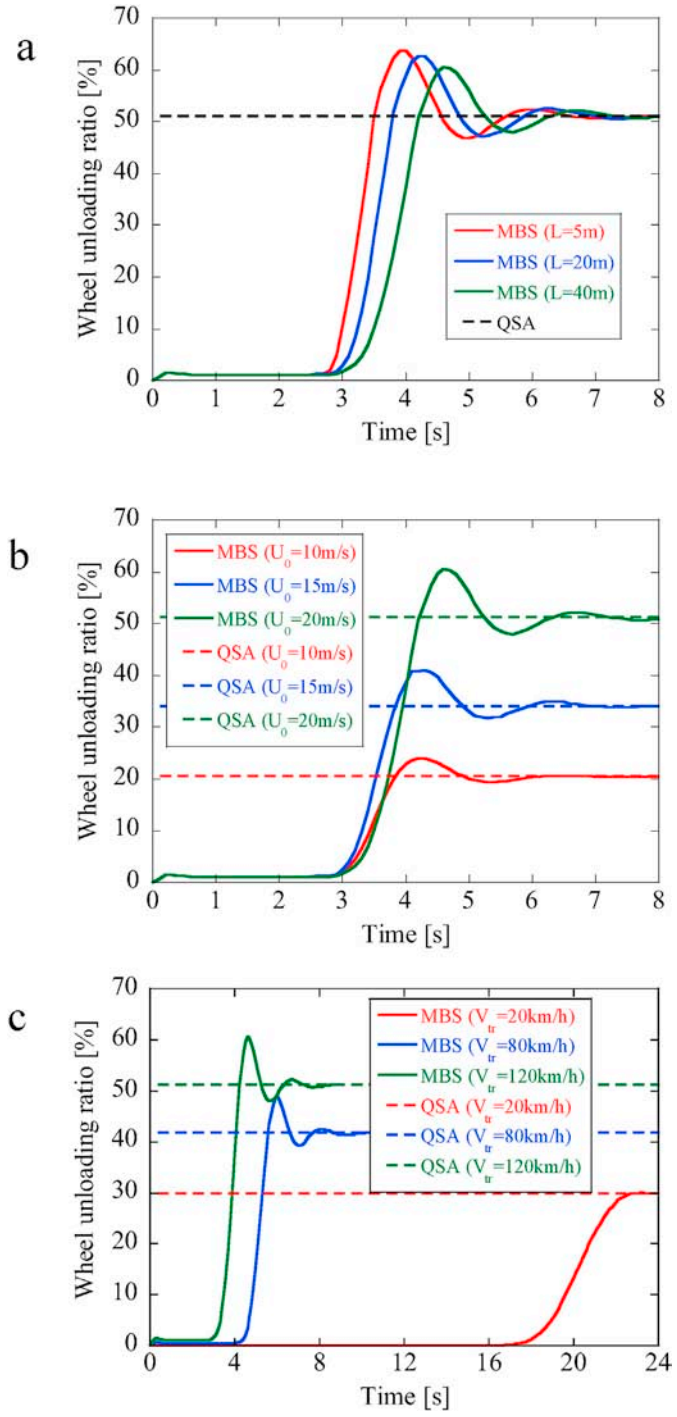


**Fig. 18.** Variations of wheel unloading ratio with: (a) gust duration ($U_0 = 20m/s,\ V_{tr} = 120km/h$); (b) gust amplitude ($L = 20m,\ V_{tr} = 120km/h$); (c) train velocity. ($L = 20m,\ U_0 = 20m/s$)

calculated by the quasi-static analysis approach to constant values obtained by multibody dynamic simulations as shown in Fig. 18. It can be concluded that the wheel unloading ratio will not be affected by these errors. Therefore, it means that the quasi-static analysis can predict the dynamic response of railway vehicles under steady winds accurately, but it may underestimate the dynamic responses if the railway vehicle is attacked by tunnel exit winds since the inertial terms and damping terms are not considered in the quasi-static analysis and they have an essential influence on the final dynamic responses of railway vehicles when the excitation changes vastly.

Furthermore, as illustrated in Fig. 18(a), wheel unloading ratio increases as the gust duration decreases since aerodynamic forces increase sharply. Wheel unloading ratio increases as either the gust amplitude or the train velocity increases, and the dynamic amplification effect becomes obvious as well in Fig. 18(b) and (c). It is interesting to note that the maximum dynamic and static wheel unloading ratios are exactly the same which means the dynamic amplification effect can be negligible if the train velocity is small enough.

Then, the DAF for the commuter rail can be obtained to describe the dynamic amplification effect after the dynamic and static wheel unloading ratios are calculated by multibody dynamic simulations and the quasi-static analysis, respectively. It is found that the dynamic amplification factor increases as the passing time $\Delta t$ defined in Eq. (35) decreases since aerodynamic forces increase to the maximum value at a shorter time, and it becomes more obvious when the passing time is smaller than 4 s in Fig. 19(a) (black points). The maximum DAF for the operational commuter rail (E233 series) is around 1.25.

As expected from Fig. 19, the DAF decreases exponentially with the passing time $\Delta t$ and a simple formula for the DAF is proposed as:

$$DAF = e^{\left[-a(\Delta t)^b\right]} + 1, \quad \Delta t = (L + L_0) \Big/ V_{tr} \tag{35}$$

where $a$ and $b$ are functions of the natural frequency $f_n$ and the damping ratio $\zeta$ of railway vehicles. $\Delta t$ refers to the passing time and evaluates how long the railway vehicle totally passes through the gust duration.

To quantitatively evaluate the effect of natural frequency, five cases

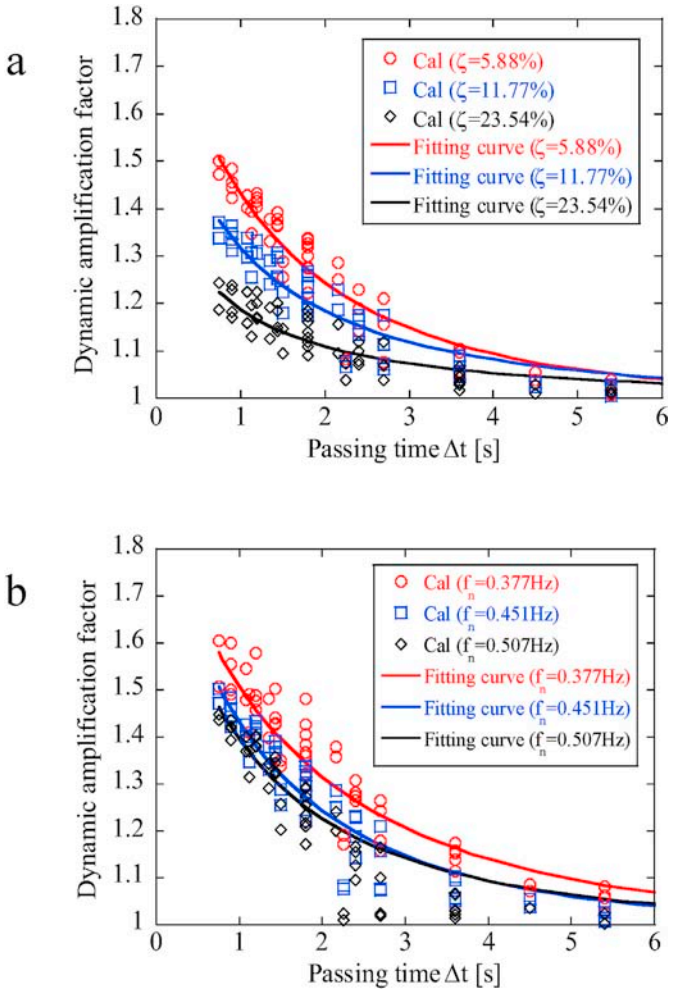


**Fig. 19.** Variations of DAF: (a) with damping ratio ($f_n = 0.451Hz$); (b) with natural frequency ($\zeta = 5.88\%$).

are studied as represented in Table 8. Case 1 shows the original vehicle parameters for the operational commuter rail. The mass of car body $m_B$ or the lateral and vertical stiffness in second suspension ($K_{ys}$, $K_{zs}$) change 0.75 or 1.25 times larger than the original value which are displayed from case 2 to case 5. The natural frequencies of railway vehicles in all cases are also calculated by the eigenvalue analysis.

Afterwards, the effect of damping ratio will be investigated since the damper can suppress the dynamic amplification effect effectively. For the operational commuter rail, dampers are installed on both primary and second suspensions. However, only the dampers in second suspension are considered mainly because aerodynamic forces act on the car body and dampers in second suspension play an essential role on the suppression of vibration. Furthermore, it is difficult to measure the damping ratio of the whole railway vehicle. In present study, the equivalent damping ratio of a railway vehicle is defined as the following equations:

$$\zeta_l = \frac{D_{ys}}{2\sqrt{4K_{ys}m_B}} \tag{36}$$

$$\zeta_v = \frac{D_{zs}}{2\sqrt{4K_{zs}m_B}} \tag{37}$$

$$\zeta = \frac{\zeta_l + \zeta_v}{2} \tag{38}$$

where $D_{ys}$ and $D_{zs}$ by Zhou et al. (2013) show damping parameters in second suspension in lateral and vertical directions, respectively. $K_{ys}$ and $K_{zs}$ are the lateral and vertical stiffness in second suspension as shown in Fig. A1, and $m_B$ represents the mass of car body. $\zeta_l$, $\zeta_v$ and $\zeta$ shown lateral, vertical and total equivalent damping ratio.

Moreover, to find an independent variable which can describe how the damping ratio affects the DAF, the total equivalent damping ratio $\zeta$ defined as Eq. (38) is proposed. In order to study the effect of damping ratio, different damping ratios are listed in Table 9. The original value of damping ratio for the operational commuter rail is represented as case 1, then 1/2 and 1/4 times as large as the original value are considered in the following cases.

In this study, five natural frequencies and three damping ratios mentioned above are considered and it means there are totally 15 cases. For every case, the DAF is calculated, and some examples are shown in Fig. 19. It is noted that the dampers can suppress the DAF effectively and the maximum DAF falls from around 1.5 to 1.25 if the damping ratio increases from 5.88% to 23.54% in Fig. 19(a). It is also found that the DAF decreases slightly as the natural frequency increases in Fig. 19(b).

Based on the numerical simulations, the fitting curves of the DAF for every case are calculated as well, and the corresponding $a$, $b$ in Eq. (35) are obtained. The relationship between $a$, $b$ in Eq. (35) and the natural frequency and equivalent damping ratio are shown in Fig. 20 in which

**Table 8**
Cases used to investigate the effect of natural frequency.

| Case | $m_B/\{m_B\}_{original}$ | $K_{ys}/\{K_{ys}\}_{original}$ | $K_{zs}/\{K_{zs}\}_{original}$ | $f_n$[Hz] |
|---|---|---|---|---|
| 1 | 1 | 1 | 1 | 0.451 |
| 2 | 0.75 | 1 | 1 | 0.508 |
| 3 | 1.25 | 1 | 1 | 0.400 |
| 4 | 1 | 0.75 | 0.75 | 0.377 |
| 5 | 1 | 1.25 | 1.25 | 0.507 |

Here, $f_n$ is obtained by eigenvalue analysis.

**Table 9**
Cases used to investigate the effect of damping ratio.

| Case | $\zeta_l$[%] | $\zeta_v$[%] | $\zeta$[%] |
|---|---|---|---|
| 1 | 25.80 | 21.28 | 23.54 |
| 2 | 12.9 | 10.64 | 11.77 |
| 3 | 6.45 | 5.32 | 5.88 |

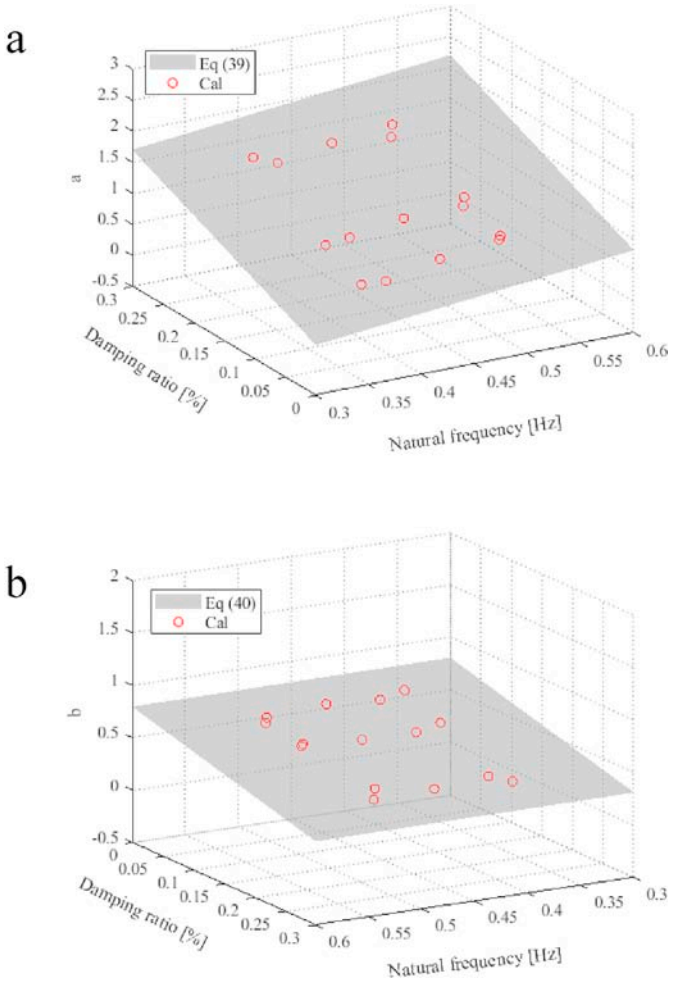


**Fig. 20.** Variations of: (a) $a(f_n, \zeta)$ and (b) $b(f_n, \zeta)$ with the damping ratio and natural frequency.

$$a(f_n, \zeta) = -0.203 + 1.714 f_n + 4.625\zeta \tag{39}$$

$$b(f_n, \zeta) = 0.818 - 0.041 f_n - 1.647\zeta \tag{40}$$

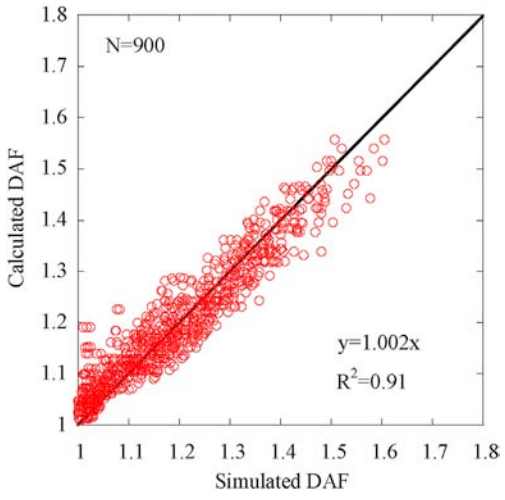


**Fig. 21.** Comparisons of the DAF obtained by simulations and Eq. (35).

they change linearly with the natural frequency and equivalent damping ratio rises. The fitting surfaces of $a$, $b$ are also calculated by the least square method, written as Eq. (39) and Eq. (40).

From now on, the DAF for railway vehicles under tunnel exit winds can be predicted by the formula Eq. (35), Eq. (39) and Eq. (40). Subsequently, the accuracy of the formula presented in Eq. (35) is studied and the DAF obtained by both calculation and prediction are shown in Fig. 21. The coefficient of determination is $R^2 = 0.91$.

## 4. Conclusions

In this study, the dynamic response of railway vehicles under tunnel exit winds is investigated by using multibody dynamic simulations and compared with the experimental data. A dynamic amplification factor for railway vehicles under tunnel exit winds is proposed and systematically investigated. The conclusions are summarized as follows:

(1) A new gust model is proposed to calculate the wind force on the railway vehicle. The predicted aerodynamic forces under the tunnel exit wind show favorable agreement with the experiment, while those by the conventional gust model are underestimated.
(2) The unsteady responses of a model vehicle in the tunnel exit wind and a commuter rail in the natural wind are investigated by multibody dynamic simulations. The predicted rolling angles of the model vehicle and the wheel unloading ratios of the commuter rail show favorably agreement with the experimental data.
(3) The dynamic amplification factor is proposed to evaluate the effect of the unsteady response on the wheel unloading ratio of railway vehicle under tunnel exit winds. It is found that the DAF decreases as the passing time as well as the damping ratio and the natural frequency of railway vehicle increase. A simple formula is also proposed to predict the DAF of railway vehicle under tunnel exit winds.

## CRediT authorship contribution statement

**Takeshi Ishihara:** Resources, Conceptualization, Methodology, Supervision, Writing - review & editing. **Dongqin Zhang:** Investigation, Software, Writing - original draft, Formal analysis, Visualization. **Yosuke Nagumo:** Data curation, Validation.

## Declaration of competing interest

The authors declare that they have no known competing financial interests or personal relationships that could have appeared to influence the work reported in this paper.

## Acknowledgements

This study is carried out as a joint research program supported by East Japan Railway Company. The authors would like to acknowledge Dr. Yu Hibino for providing the experimental data and figures of the running vehicle test and Dr. Yayoi Misu for providing the measurement data of the field test.

## Appendix A. Identification of structural parameters of the model vehicle and the sinusoidal lateral force

The stiffness of vertical bump stop, lateral and vertical dampers of the model vehicle are unknown in Hibino el al. (2013a). The measurement equipment is installed in the car body, which pushes the car body downwards and decreases the vertical bump stop clearance as shown in Fig. A1. Furthermore, although there is no damper installed in the scale model vehicle, the decay in the free vibration is observed, which means that the damping effect exits in the model vehicle. In this study, the same lateral and vertical dampers are added in the second suspension to simulate the observed structural damping. The stiffness ($K_{zs2}$) and the damping value ($D_{ys}, D_{zs}$) which are shown in Fig. A1 are identified to update the numerical model.

Fig. A2 illustrates the flowchart of parameter identification. The multibody vehicle model is built with two unknown parameters defined by two arbitrary initial values. The natural frequency and damping ratio are then obtained from the simulations. Bisection method is adopted to update the unknown parameters and reduce the relative errors between the identified natural frequency and damping ratio and experimental data. The iteration will stop until the relative errors are smaller than 1%. Table A1 shows comparisons of the initial, identified and measured parameters. The natural frequency identified from the time series of roll motion is higher than that by eigenvalue analysis since the effects of nonlinear spring and damping are not included in eigenvalue analysis.

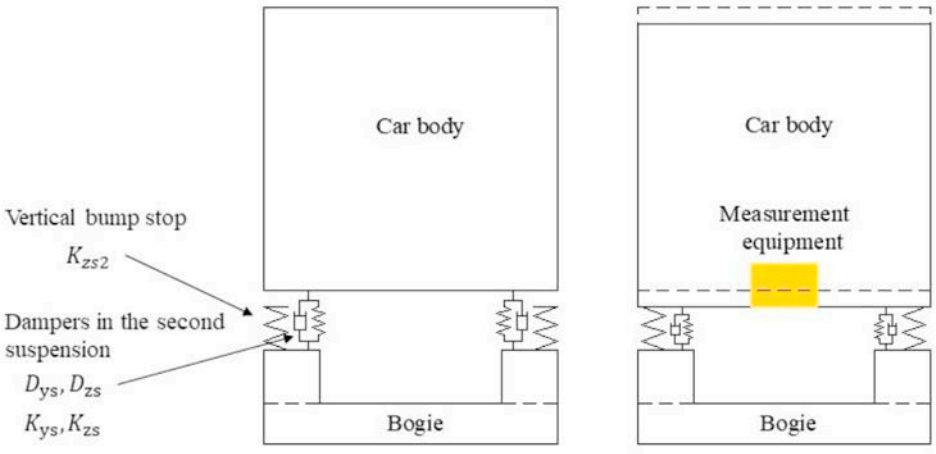


**Fig. A1.** Vertical movement of car body: (a) original position; (b) downward movement.

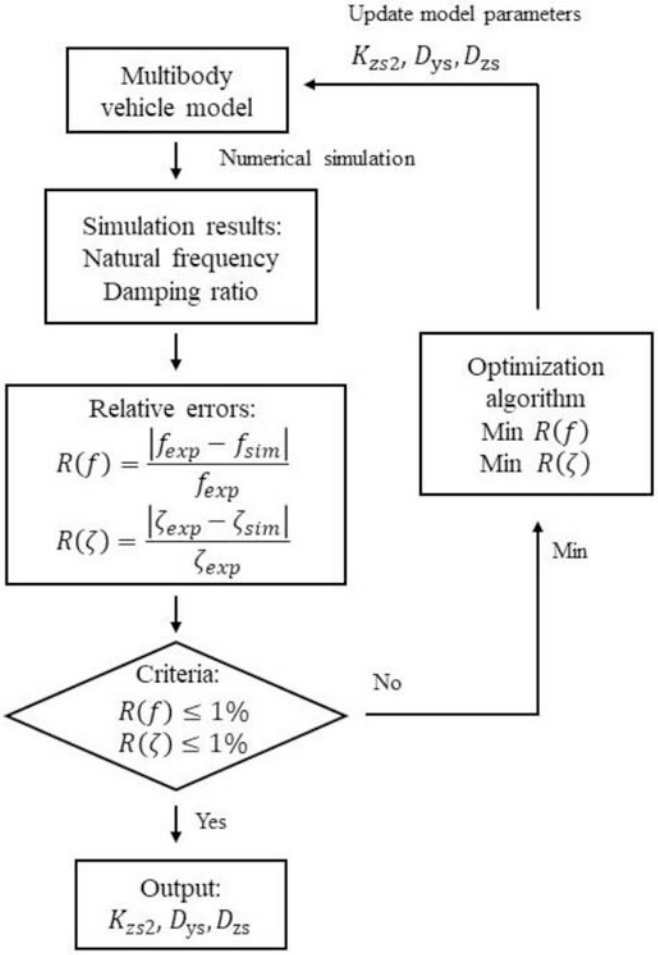


**Fig. A2.** Flowchart of parameter identification for the structural parameters of the model vehicle.

**Table A1**
Comparisons of the initial, identified and measured parameters (structural parameters of the model vehicle)

| Parameter | $K_{zs2}$ $[N/m]$ | Natural frequency $[Hz]$ | Relative error [%] | $D_{ys}$, $D_{zs}$ $[N \cdot s/m]$ | Damping ratio [%] | Relative error [%] |
|---|---|---|---|---|---|---|
| Initial | 15,000 | 2.182 (1.711) | 8.0 | 158 | 6.43 | 60.8 |
| Identified | 750 | 2.018 (1.581) | 0.2 | 94 | 4.01 | 0.3 |
| Measured | – | 2.014 | – | – | 4.00 | – |

The numbers in parentheses indicate the values obtained by eigenvalue analysis. The natural frequency identified from the time series for rolling motion and that obtained by eigenvalue analysis in full scale are 0.638 and 0.500, respectively.

In order to simulate the track irregularity, the sinusoidal lateral force is assumed as shown in Eq. (A1) where there are three unknown parameters $A_{sl}$, $B_{sl}$ and $C_{sl}$, which influence on the amplitude, period and phase of the rolling angle of car body and are identified using the rolling angle of car body in the no wind region as shown in Fig. 11(a). The averaged amplitude and period of the rolling angle listed in Table A2 are calculated using the three vibration periods from 8s to 10s since the model vehicle is mainly affected by the track irregularity at this moment. $A_{sl}$ and $B_{sl}$ are identified by the averaged amplitude and period of the rolling angle as shown in Fig. A3. The unknown parameters $A_{sl}$ and $B_{sl}$ are updated by the bisection method and the relative errors between the identified amplitude and period and experimental data are reduced until the relative errors smaller than 1%. Table A2 shows comparisons of the initial, identified and measured parameters. $C_{sl} = 3.338\ radian$ is identified when the simulated and experimental rolling angle coincide in the last period.

$$F_V^{'} = A_{sl} sin(2\pi B_{sl} t + C_{sl}) \tag{A1}$$

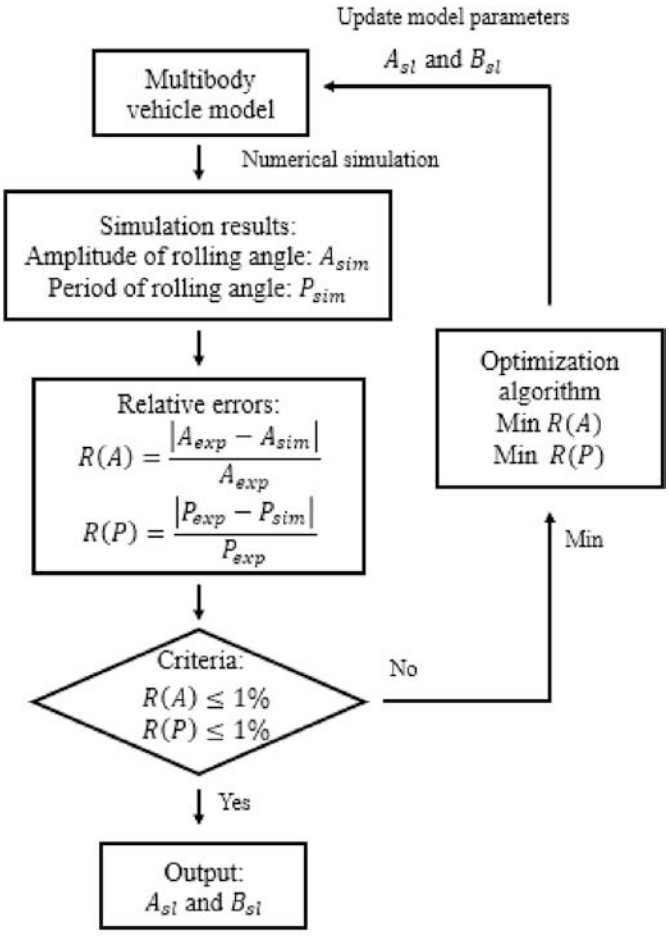


**Fig. A3.** Flowchart of parameter identification for the sinusoidal lateral force.

**Table A2**
Comparisons of the initial, identified and measured parameters (the sinusoidal lateral force)

| Parameter | $A_{sl}$ [$N$] | Amplitude of rolling angle [*degree*] | Relative error [%] | $B_{sl}$[Hz] | Period of rolling angle [$s$] | Relative error [%] |
|---|---|---|---|---|---|---|
| Initial | 0.2 | 0.105 | −47.5 | 1.897 | 0.528 | 1.8 |
| Identified | 0.208 | 0.168 | 0.0 | 1.976 | 0.506 | 0.6 |
| Measured | – | 0.168 | – | – | 0.503 | – |

## Appendix B. Three-second averaged wind speed method

The 3-s averaged wind speed method was proposed by Nagumo and Ishihara (2020) and was validated by the field test reported by Suzuki and Hibino (2016). Fig. B1 shows the overview of field test, in which three anemometers were installed on the windward side to measure the turbulent winds and load cells were set up under the wheels to measure aerodynamic forces.

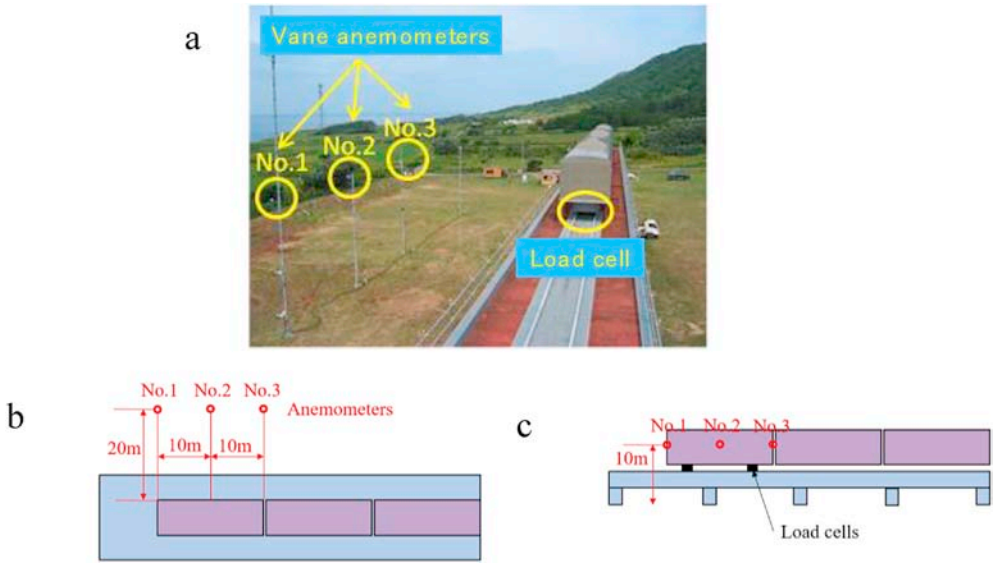


**Fig. B1.** Overview of field test and location of anemometers and load cells: (a) overview; (b) top view; (c) side view.

The spatial averaged wind speed $u_{sa}(t)$ is estimated by

$$u_{sa}(t) = \sqrt{\frac{\sum_{i=1}^{3} u_{i,\,inst}^2(t)}{3}} \tag{B1}$$

where $u_{i,\,inst}$ denotes the instantaneous wind speed by the $i$th anemometer.

Three-second averaged wind speed $v_{3s-gust}(t)$ is calculated by

$$u_{3s-gust}(t) = \frac{\sum_{i=1}^{6} u_{2,\,inst}\left(t - 3 + \frac{i}{2}\right)}{6} \tag{B2}$$

where $u_{2,\,inst}$ refers to the instantaneous wind speed on the No. 2 anemometer. The data sampling rate is 2 Hz.

The aerodynamic forces are calculated by Eq. (7) (8) and (9) based on the different wind speeds. The overturning moment on the leeward wheel is estimated by

$$M_{O.C}(t) = F_S(t)h_c + F_L(t)\frac{G}{2} + M_R(t) \tag{B3}$$

where $h_c$ is the height of center of car body and $G$ is distance between two wheel-rail contact points as shown in Fig. B2.

The calculated overturning moments are compared with the measurements to evaluate the accuracy of aerodynamic forces calculated by the different wind speeds. The ratio of the maximum measured and calculated overturning moment at every 60 s is calculated by

$$R(T) = \frac{Max[M_{O.M}(T)]}{Max[M_{O.C}(T)]} \tag{B4}$$

where $M_{O.M}(T)$ and $M_{O.C}(T)$ are the measured and calculated overturning moments as illustrated in Fig. B2. The time interval $T$ is 60 s.

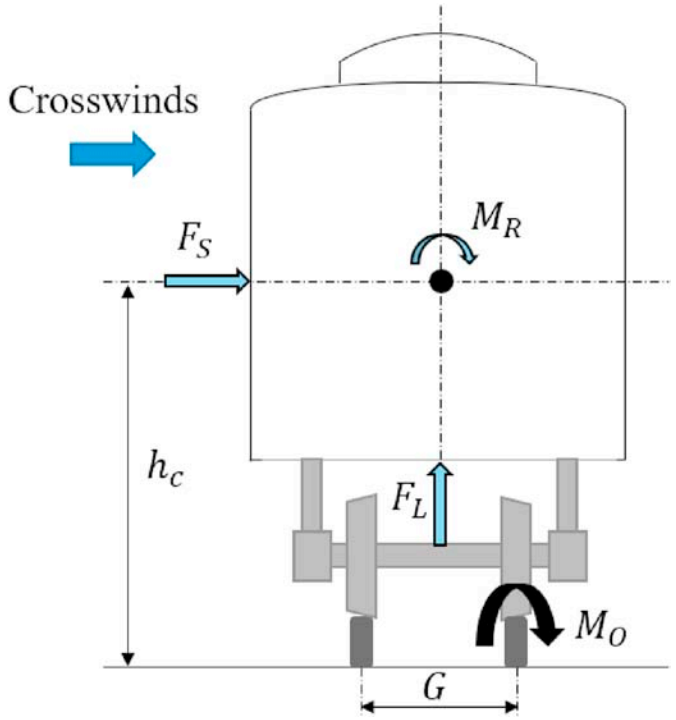


**Fig. B2.** Description of aerodynamic forces and the overturning moment.

Fig. B3 shows the frequency distribution of the ratio of the measured and calculated overturning moment based on 720 datasets. $u_{\mathrm{inst}}$, $u_{sa}$ and $u_{3s-\mathrm{gust}}$ express the instantaneous, spatial averaged and 3-s averaged wind speeds, respectively. It is found that the mean value of the ratio calculated by the instantaneous wind speed is less than 1, while the frequency distribution of the ratio calculated by the 3-s averaged wind speed show good agreement with those by the spatial averaged wind speed. It implies that the spatial average effect, namely, size reduction is included in the calculated overturning moment by the 3-s averaged wind speed.

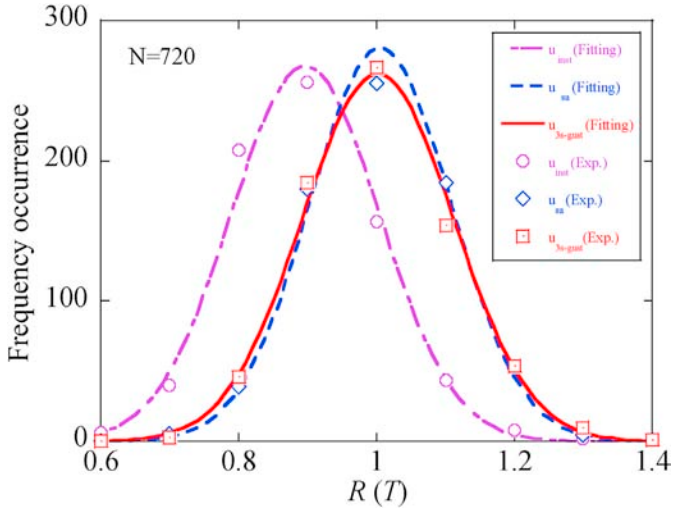


**Fig. B3.** Frequency distribution of the ratio of the maximum measured and calculated overturning moment.

The time series of the measured instantaneous wind speeds are used in Appendix B and Section 3.2. The maximum value of 3-s averaged wind speed during 60 s is used in QSA to predict the characteristic force, while the 60 s time series of 3-s averaged wind speed is adopted in MBS to calculate the buffeting force and dynamic response of the vehicle.

## References

Baker, C., 2013. A framework for the consideration of the effects of crosswinds on trains. J. Wind Eng. Ind. Aerod. 123, 130–142.
Baker, C., Cheli, F., Orellano, A., Paradot, N., Proppe, C., Rocchi, D., 2009. Cross-wind effects on road and rail vehicles. Veh. Syst. Dyn. 47, 983–1022.
Baker, C.J., Jones, J., Lopez-Calleja, F., Munday, J., 2004. Measurements of the cross wind forces on trains. J. Wind Eng. Ind. Aerod. 92, 547–563.
Bocciolone, M., Cheli, F., Corradi, R., Muggiasca, S., Tomasini, G., 2008. Crosswind action on rail vehicles: wind tunnel experimental analyses. J. Wind Eng. Ind. Aerod. 96, 584–610.

Brady, S.P., O'Brien, E.J., 2006. Effect of vehicle velocity on the dynamic amplification of two vehicles crossing a simply supported bridge. J. Bridge Eng. 11, 250–256.
Carrarini, A., 2008. Efficient models and techniques for the computational analysis of railway vehicles in crosswinds. Veh. Syst. Dyn. 46, 77–86.
Carrarini, A., 2007. Reliability based analysis of the crosswind stability of railway vehicles. J. Wind Eng. Ind. Aerod. 95, 493–509.
Cheli, F., Corradi, R., Tomasini, G., 2012. Crosswind action on rail vehicles: a methodology for the estimation of the characteristic wind curves. J. Wind Eng. Ind. Aerodyn. 104–106, 248–255.
Cheli, F., Giappino, S., Rosa, L., Tomasini, G., Villani, M., 2013. Experimental study on the aerodynamic forces on railway vehicles in presence of turbulence. J. Wind Eng. Ind. Aerod. 123, 311–316.
Cheli, F., Ripamonti, F., Rocchi, D., Tomasini, G., 2010. Aerodynamic behaviour investigation of the new EMUV250 train to cross wind. J. Wind Eng. Ind. Aerod. 98, 189–201.
Dassault Systems, 2017. SIMPACK 2017.1 Simpack Assistant.
Dorigatti, F., Sterling, M., Baker, C.J., Quinn, A.D., 2015. Crosswind effects on the stability of a model passenger train-A comparison of static and moving experiments. J. Wind Eng. Ind. Aerod. 138, 36–51.
EN 14067-6, 2010. Railway Applications - Aerodynamics - Part 6: Requirements and Test Procedures for Cross Wind Assessment, European Committee for Standard.
Hibino, Y., Kanemoto, H., Sakuma, Y., 2011a. Analysis of Railway Vehicle Dynamics Affected by Crosswinds (Part 1-outline of Running Tests under Crosswinds Using a 1/tenth Scale Model) (RAIL2011).
Hibino, Y., Kanemoto, H., Sakuma, Y., 2013a. A study on vehicle response to a sudden gust of wind. Trans. Jpn. Soc. Mech. Eng. Ser. C 79, 3410–3419 (in Japanese).
Hibino, Y., Kanemoto, H., Shimomura, 2013b. Safety evaluation of railway vehicle against crosswind applying a full-vehicle simulation model. Q. Rep. RTRI 54 (3), 133–138.
Hibino, Y., Misu, Y., Kurihara, T., Moriyama, A., Shimamura, M., 2011b. Study of new methods for train operation control in strong winds. JR EAST Tech. Rev. 19, 31–36.
Hibino, Y., Shimomura, T., Tanifuji, K., 2010. Full-scale experiment on the behavior of a railway vehicle being subjected to lateral force. J. Mech. Syst. Transport. Logist. 3, 35–43.
Hoblit, F.M., 1988. Gust Loads on Aircraft: Concepts and Applications. AIAA, Washington DC.
Hu, P., Han, Y., Cai, C.S., Cheng, W., Lin, W., 2019. New analytical models for power spectral density and coherence function of wind turbulence relative to a moving vehicle under crosswinds. J. Wind Eng. Ind. Aerod. 188, 384–396.
IEC 61400-1, 2019. Wind Turbine Generator Systems Part 1, Safety Requirements. International Electrotechnical Commission.
Imai, T., Fujii, T., Tanemoto, K., Shimamura, T., Maeda, T., Ishida, H., Hibino, Y., 2002. New train regulation method based on wind direction and velocity of natural wind against strong winds. J. Wind Eng. Ind. Aerod. 90, 1601–1610.
Iwnicki, S., 2006. Handbook of Railway Vehicle Dynamics. CRC Press.
Kikuchi, K., Suzuki, M., 2015. Study of aerodynamic coefficients used to estimate critical wind speed for vehicle overturning. J. Wind Eng. Ind. Aerod. 147, 1–17.
Li, X.-Z., Xiao, J., Liu, D.-J., Wang, M., Zhang, D.-Y., 2017. An analytical model for the fluctuating wind velocity spectra of a moving vehicle. J. Wind Eng. Ind. Aerod. 164, 34–43.
Liu, D., Wang, Q., Zhong, M., Lu, Z., Wang, J., Wang, T., Lv, S., 2019. Effect of wind speed variation on the dynamics of a high-speed train. Veh. Syst. Dyn. 57, 247–268.
Liu, D., Wang, T., Liang, X., Meng, S., Zhong, M., Lu, Z., 2020. High-speed train overturning safety under varying wind speed conditions. J. Wind Eng. Ind. Aerod. 198, 104111.
Liu, Z., Zhang, C., Ishihara, T., 2018. Numerical study of the wind loads on a cooling tower by a stationary tornado-like vortex through LES. J. Fluid Struct. 81, 656–672.
Nagumo, Y., Ishihara, T., 2020. A study of crosswind resistant performance of train cars considering uncertainties of acting forces. J. Wind Eng. 45, 79–92 (in Japanese).
Premoli, A., Rocchi, D., Schito, P., Tomasini, G., 2016. Comparison between steady and moving railway vehicles subjected to crosswind by CFD analysis. J. Wind Eng. Ind. Aerod. 156, 29–40.
Schober, M., Weise, M., Orellano, A., Deeg, P., Wetzel, W., 2010. Wind tunnel investigation of an ICE 3 endcar on three standard ground scenarios. J. Wind Eng. Ind. Aerod. 98, 345–352.
Sesma, I., Vinolas, J., San Emeterio, A., Gimenez, J.G., 2012. A comparison of crosswind calculations using a full vehicle and a simplified 2D model. Proc. Inst. Mech. Eng. - Part F J. Rail Rapid Transit 226, 305–317.
Sterling, M., Baker, C., Bouferrouk, A., ONeil, H., Wood, S., Crosbie, E., 2009. An investigation of the aerodynamic admittances and aerodynamic weighting functions of trains. J. Wind Eng. Ind. Aerod. 97, 512–522.
Suzuki, M., Hibino, Y., 2016. Field tests and wind tunnel tests on aerodynamic characteristics of train/vehicles under crosswinds. Q. Rep. RTRI 57, 55–60.
Thomas, D., Berg, M., Stichel, S., 2010a. Measurements and simulations of rail vehicle dynamics with respect to overturning risk. Veh. Syst. Dyn. 48, 97–112.
Thomas, D., Berg, M., Stichel, S., Diedrichs, B., 2015. Rail vehicle response to lateral carbody excitations imitating crosswind. Proc. Inst. Mech. Eng. - Part F J. Rail Rapid Transit 229, 34–47.
Thomas, D., Diedrichs, B., Berg, M., Stichel, S., 2010b. Dynamics of a high-speed rail vehicle negotiating curves at unsteady crosswind. Proc. Inst. Mech. Eng. - Part F J. Rail Rapid Transit 224, 567–579.
Tomasini, G., Cheli, F., 2013. Admittance function to evaluate aerodynamic loads on vehicles: experimental data and numerical model. J. Fluid Struct. 38, 92–106.
You, W., Kwon, H., Park, J., Shin, Y., 2018. Effect of wind gusts on the dynamics of railway vehicles running on a curved track. Proc. Inst. Mech. Eng. - Part F J. Rail Rapid Transit 232, 1103–1120.
Zhai, W., Xia, H., Cai, C., Gao, M., Li, X., Guo, X., Zhang, N., Wang, K., 2013. High-speed train–track–bridge dynamic interactions – Part I: theoretical model and numerical simulation. Int. J. Rail Transport. 1, 3–24.
Zhou, S., Tao, Y., Zhang, Z., Yang, J., 2013. SIMPACK 9 Tutorial. Beijing Union Press (in Chinese).